Available online at www.sciencedirect.com
ScienceDirect
Journal of Computational Physics 225 (2007) 840–873
JOURNAL OF COMPUTATIONAL PHYSICS
www.elsevier.com/locate/jcp

A robust and accurate approach to computing compressible multiphase flow: Stratified flow model and AUSM$^+$-up scheme

Chih-Hao Chang [a,*], Meng-Sing Liou [b]

[a] Center for Risk Studies and Safety, University of California, Santa Barbara, Goleta, CA 93117, USA
[b] Propulsion Systems Division, NASA Glenn Research Center, Cleveland, OH 44135, USA

Received 25 February 2006; received in revised form 21 December 2006; accepted 4 January 2007
Available online 19 January 2007

Abstract

In this paper, we propose a new approach to compute compressible multifluid equations. Firstly, a single-pressure compressible multifluid model based on the stratified flow model is proposed. The stratified flow model, which defines different fluids in separated regions, is shown to be amenable to the finite volume method. We can apply the conservation law to each subregion and obtain a set of balance equations[1]. Secondly, the AUSM$^+$ scheme, which is originally designed for the compressible gas flow, is extended to solve compressible liquid flows. By introducing additional dissipation terms into the numerical flux, the new scheme, called AUSM$^+$-up, can be applied to both liquid and gas flows. Thirdly, the contribution to the numerical flux due to interactions between different phases is taken into account and solved by the exact Riemann solver. We will show that the proposed approach yields an accurate and robust method for computing compressible multiphase flows involving discontinuities, such as shock waves and fluid interfaces. Several one-dimensional test problems are used to demonstrate the capability of our method, including the Ransom's water faucet problem and the air–water shock tube problem. Finally, several two dimensional problems will show the capability to capture enormous details and complicated wave patterns in flows having large disparities in the fluid density and velocities, such as interactions between water shock wave and air bubble, between air shock wave and water column(s), and underwater explosion.
© 2007 Elsevier Inc. All rights reserved.

PACS: 83.85.Pt; 47.11.+j; 47.55.Kf

Keywords: Multiphase flow; Multifluid model; AUSM$^+$ scheme; Stratified flow method

1. Introduction

Seeking an accurate method to simulate compressible multifluid and multiphase flows has been an important research topic for many engineering applications. Examples of compressible multifluid flows include the

* Corresponding author.
E-mail addresses: chchang@engineering.ucsb.edu (C.-H. Chang), meng-sing.liou@grc.nasa.gov (M.-S. Liou).

[1] However, conservative form is lost in these balance equations when considering each individual phase; in fact, the interactions that exist simultaneously in both phases manifest themselves as nonconservative terms.

0021-9991/$ - see front matter © 2007 Elsevier Inc. All rights reserved.
doi:10.1016/j.jcp.2007.01.007

cooling system in the conventional nuclear reactor, the fuel transport system in which the fuel and gas are transported simultaneously, and the generation, deformation and collapse of cavities around the underwater propeller or within the high pressure injector. The flow phenomena involved in these systems are very complicated, entailing reliable mathematical description (modeling) and numerical methods.

In this paper, we will concentrate on the numerical algorithm for compressible multifluid equations in which the fluids are assumed inter-penetrating, non-homogeneous and non-equilibrium; that is, each fluid has its own velocity and temperature fields at the same location, but all fluids share the same pressure. As shown by Buyevich [1] and Ishii [2], one can use two sets of Euler/Navier–Stoke equations to describe the motion of gas and liquid phase fluids respectively, as given in the following:

$$\begin{aligned}
&\frac{\partial(\alpha_i\rho_i)}{\partial t} + \nabla\cdot(\alpha_i\rho_i\vec{v}_i) = S_\rho,\\
&\frac{\partial(\alpha_i\rho_i\vec{v}_i)}{\partial t} + \nabla\cdot(\alpha_i\rho_i\vec{v}_i\vec{v}_i) + \nabla(\alpha_i p) = p\nabla\alpha_i + \vec{S}_v,\\
&\frac{\partial(\alpha_i\rho_i E_i)}{\partial t} + \nabla\cdot(\alpha_i\rho_i H_i\vec{v}_i) = -p\frac{\partial\alpha_i}{\partial t} + S_e,
\end{aligned} \tag{1}$$

where the subscript "i"="g" or "l", representing gas or liquid phase fluid respectively. α_i is the void fraction of fluid "i", and must satisfy the constraint, $\alpha_g + \alpha_l = 1$. The RHS of Eq. (1) represents the interactions that couple both fluid motions together. The "S" terms on the right hand side represent a group of terms that arise from interfacial physics, viscous effects, phase change, body forces, etc. They are expressed in differential (first or higher derivatives) or non-differential form. The system of equations is quite general and has been widely used to describe multiphase flows in a variety of applications. However, the inviscid limit of the multifluid model has been known to be problematic, giving rise to instability, loss of accuracy, and non-convergence in numerical solution. It is primarily attributable to the fact that the system can become non-hyperbolic and ill-posed. Hence, the root of the problems points to the first derivative terms that differ from that for the single fluid equations (which are known to be hyperbolic), namely, $p\nabla\alpha_i$ and $-p\frac{\partial\alpha_i}{\partial t}$. Additionally, these terms are not in conservative form. It is not clear that a discontinuity in the sense of weak solution still remains valid. Some comprehensive reviews of the compressible multifluid models can be found in [3,4].

It has been recognized that non-hyperbolicity is a major reason for causing numerical instability. Thus, a great deal of efforts have been focused on how to improve the hyperbolicity of the system and make the multifluid equations well-posed; clearly altering first derivative terms with some physical basis is necessary, such as interfacial pressure correction [5], virtual mass [6], or separate pressures [3,7]. However, we will show that non-hyperbolicity is not the only reason for causing numerical instability. It is as important to properly handle the discretization and define numerical fluxes that includes all relevant interactions terms between the same and different phases in order to obtain a stable and accurate numerical solution.

To highlight the importance of a numerical method for solving a multifluid model, we consider the case of an 1D moving fluid interface with constant velocity and pressure. Since all convection fluxes cancel out with each other, Eq. (1) reduces to a simple equation that the numerical solution must satisfy the so called *pressure non-disturbing condition* [7] given as follows:

$$\nabla(\alpha_i p) = p\nabla\alpha_i. \tag{2}$$

The LHS of the above equation is in conservative form and similarly exists in the single fluid equations, hence it is rather clear what to do about its discretization. However, it is not so obvious how to discretize the RHS term, $\nabla\alpha_i$, which is in nonconservative form, because it will have to be compatible with how the pressure flux $\alpha_i p$ is evaluated in order to satisfy the above equation. For example, a central differencing of $\nabla\alpha_i$ is unlikely to be compatible with an upwind differencing of $\nabla(\alpha_i p)$. On the other hand if the discretization of the LHS requires analytical form of the eigenstructure of Eq. (1), which unfortunately is not available in general, then it will be difficult to come up with a compatible RHS.

While Eq. (1) is usually derived from an averaging procedure [1,2], Stewart and Wendroff [3] gave another approach for derivation based on the stratified flow model. Adopting the concept of the stratified flow model has several advantages. Firstly, it gives a clear view of the mathematical representation of physics involved in multifluid flow. Secondly, we find that it provides a clue as to the construction of numerical fluxes. It has led us

to recognize various types of interactions, not only that occurring within a cell between different phases, but also that at the cell boundaries, as illustrated in Fig. 1. The former is the in-cell interaction that gives rise to the nonconservative term in Eq. (2), marked by **A**. The latter, marked by **B** in Fig. 1b, is a natural consequence of the finite volume method and is consistent with the stratified model; it is however not observed previously in the literature. We refer these interactions due to different phases collectively to as inter-phasic terms. We first explore the stratified flow model in our earlier paper [8] and further refine the numerical procedure in [9] by including the Riemann solver and applications to various problems. Independently, the idea of recognizing the presence of different phases in each sub-volume appears in [10]. Their method is further employed for different studies [11,12] in the multifluid framework.

To our knowledge, all numerical methods for multifluid flows are extended from the ones for single fluid. The extension is not necessarily straightforward; in fact, difficulties arise because we need be concerned with additional issues. These include: (1) disparities in fluid velocities and properties, (2) non-hyperbolicity of the partial differential equations, (3) terms in nonconservative form, (4) surface tension force, etc. The manifestation of difficulties can be in stability, accuracy (e.g., unwanted oscillations and smearing), or uniqueness of solution. Moreover, even if the multifluid model is rendered hyperbolic, its eigensystem is still too complicated to be put in an analytical form, hence making it difficult to use the characteristic-based approximate Riemann solvers such as the Roe's scheme or the Osher's scheme. On the other hand, the simplicity of the flux vector splitting scheme [13] or the AUSM-family schemes [14] makes them an attractive alternative for the current multifluid model.

The AUSM$^+$ scheme proposed by Liou [15] is known to be accurate and robust for compressible gas flows, especially for its ability in capturing shock and contact discontinuities. It can be easily extended to multispecies equations, and it can also handle flows of very low Mach number with the help of a pre-conditioning matrix and the numerical speed of sound [16]. While being successful for computing gas flows, the AUSM$^+$ scheme is found to yield oscillatory solutions for liquid fluid, for which the equation of state, such as the stiffened gas model [17] or the Tait's model, is stiff. To overcome this problem due to stiffness, new diffusion terms based on the pressure and velocity fields are introduced to the AUSM$^+$ scheme [8,18]. The modified scheme is essentially a variation of the AUSM$^+$-up scheme of Liou [14,19]. These diffusion terms are used to enhance the coupling between the pressure and velocity fields. We will show that they can effectively suppress numerical oscillations behind the pressure waves.

The rest of the paper is organized as follows. Section 2 shows the details of our method. We will discuss the stratified flow model, the discretization, the AUSM$^+$-up scheme, exact Riemann solver for gas–liquid inter-

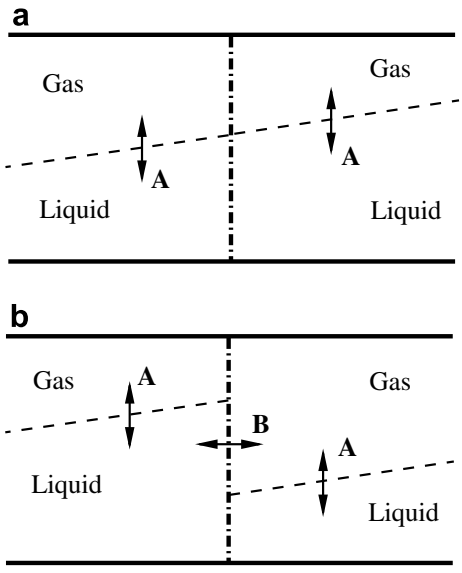

Fig. 1. Illustration of the inter-phasic terms between different phases.

face, the interfacial pressure correction, the updating procedure, and the extension to multidimensional flows. Section 3 presents results of several 1D and 2D problems. Finally, concluding remarks are given in Section 4.

2. Numerical method

In this section, we shall present the conservation laws based on the stratified flow model, its discrete counterpart and the numerical method. We begin by defining the control volume of each phase and identifying interfaces between the same and different fluids on the control surface. Then, we shall introduce the AUSM$^+$-up scheme and the exact Riemann solver we use to calculate the numerical flux. In addition, we will discuss how the interfacial pressure correction term, which is included to make the system hyperbolic, will be incorporated in our framework. Finally, the updating of variables requires additional attention.

2.1. The stratified flow model

By adopting the concept of stratified model [3][2], we find several advantages. It gives a clear physical interpretation of the interfacial terms manifesting the interactions between phases and it allows an easy procedure to balance the pressure terms, Eq. (2). We also show that the inviscid limit of Eq. (1) can be derived by the the stratified flow model. As illustrated in Fig. 2, two different fluids, delineated by the void fraction function α_i, are conceptually considered to occupy in two separate regions. Within each region, a single fluid (phase) is defined, with its properties and flow variables clearly identifiable. Hence, it is straightforward to apply the conservation laws to each fluid, say fluid "i", in partial control volume V_i of the total volume V,

$$\begin{aligned}
&\frac{\partial}{\partial t}\int_{V_i}\rho_i\,\mathrm{d}V_i+\oint_{S_i}(\rho_i\vec{v}_i)\cdot\vec{n}\,\mathrm{d}S_i=0,\\
&\frac{\partial}{\partial t}\int_{V_i}\rho_i\vec{v}_i\,\mathrm{d}V_i+\oint_{S_i}(\rho_i\vec{v}_i\vec{v}_i)\cdot\vec{n}\,\mathrm{d}S_i+\oint_{S_i}p\vec{n}\,\mathrm{d}S_i=0,\\
&\frac{\partial}{\partial t}\int_{V_i}\rho_iE_i\,\mathrm{d}V_i+\int_V p\frac{\partial\alpha_i}{\partial t}\,\mathrm{d}V+\oint_{S_i}(\rho_iH_i\vec{v}_i)\cdot\vec{n}\,\mathrm{d}S_i=0,
\end{aligned}\tag{3}$$

where $V_i=\alpha_iV$ and S_i is the surface area enclosing V_i. It is noted that the above integral equations appear in conservative form, as in the case of single phase flow. When expressed in differential form, it can be shown that in the inviscid limit and ignoring body and surface forces, the above equations are equivalent to Eq. (1) if α_i is continuous because $V_i=\alpha_iV$ is varying with space and time.

To close this system with equal numbers of unknown variables and equations, it is necessary to supplement with equations of state and the constraint $\alpha_g+\alpha_l=1$. In this paper, we assume that the gas and liquid phases are respectively described by the ideal gas and stiffened gas equations of state. The latter is given in Appendix A.

For clarity, we will first develop the numerical method for the 1D system and then extend it for the multidimensional system. In what follows, we will consider the discretization of Eq. (3) for a stationary (Eulerian) cell located in the closed interval $[x-\triangle x/2,x+\triangle x/2]$. Making appropriate substitutions of the partial volume with the total volume, the surface integral now is broken into two parts: (1) the usual flux integral evaluated at the cell boundaries $x\pm\triangle x/2$, and (2) the additional one arising at the in-cell interface (volume-fraction line). Since there is not a net flow crossing the in-cell interface, there is no convective flux and pressure is the only force exerted there. Thus, the final equations become

$$\frac{\partial}{\partial t}\int_{x-\frac{\Delta x}{2}}^{x+\frac{\Delta x}{2}}\begin{pmatrix}\alpha_i\rho_i\\ \alpha_i\rho_iu_i\\ \alpha_i\rho_iE_i\end{pmatrix}\mathrm{d}x+\int_{x-\frac{\Delta x}{2}}^{x+\frac{\Delta x}{2}}\frac{\partial}{\partial x}\begin{pmatrix}\alpha_i\rho_iu_i\\ \alpha_i(\rho_iu_i^2+p)\\ \alpha_i\rho_iu_iH_i\end{pmatrix}\mathrm{d}x+\int_{x-\frac{\Delta x}{2}}^{x+\frac{\Delta x}{2}}p\begin{pmatrix}0\\ 0\\ \frac{\partial\alpha_i}{\partial t}\end{pmatrix}\mathrm{d}x-\int_{x-\frac{\Delta x}{2}}^{x+\frac{\Delta x}{2}}p\begin{pmatrix}0\\ \frac{\partial\alpha_i}{\partial x}\\ 0\end{pmatrix}\mathrm{d}x=0.\tag{4}$$

[2] Here we do not require that the fluid be physically stratified; we use the concept only to facilitate the derivation of the multifluid model in an average sense, and more importantly the discretization of numerical fluxes.

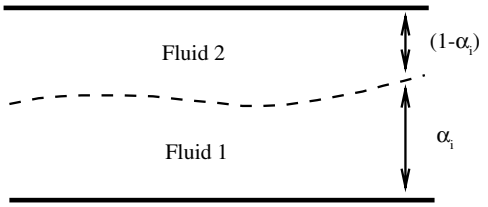

Fig. 2. Illustration of the stratified flow.

The second term is similar to the typical flux for the single phase flow, except each phase now contributes a portion corresponding to its volume fraction α_i. Additional terms reflect interactions due to the presence of the other fluid. The third term is the work done to phase "i" due to its volume change and the last term represents the force exerted at the in-cell interface.

2.2. The discretization of the stratified model

A general discretized form of the above equations may be expressed as

$$\frac{\triangle x}{\triangle t}\delta_t \begin{pmatrix} \alpha_i\rho_i \\ \alpha_i\rho_i u_i \\ \alpha_i\rho_i E_i \end{pmatrix}_j + \delta_x(\alpha_i \mathbf{f}_i)_j + p_j \frac{\triangle x}{\triangle t}\begin{pmatrix} 0 \\ 0 \\ \delta_t\alpha_i \end{pmatrix}_j - p_j \begin{pmatrix} 0 \\ \delta_x\alpha_i \\ 0 \end{pmatrix}_j = 0, \tag{5}$$

where $\mathbf{f}$ is the numerical flux having an identical expression as for single phase flow,

$$\mathbf{f} = (\rho u, \rho u^2 + p, \rho u H)^{\mathrm{T}}. \tag{6}$$

The time and spatial difference operators are: $\delta_t(\cdot) = (\cdot)^{n+1} - (\cdot)^n$ and $\delta_x(\cdot)_j = (\cdot)_{j+1/2} - (\cdot)_{j-1/2}$. Note that the integrals in Eq. (5) are accurate up to at least second order if one assumes that p and α are smooth within each cell and the pressure p_j is taken to be the cell-averaged value.

With the finite volume method, the flow variables are described by a piecewise function within the cell and may be discontinuous at the cell boundaries. Using the reconstructed volume-fraction function and following the framework of the stratified model, the flow configuration, which now contains an *internal* (within each cell) structure separating both fluids in the cell, is depicted in Fig. 3, with gas in $(\overline{acgh})$ and liquid in $(\overline{cdef})$. That is, one can express a discontinuous change at the interface between phases via the volume fraction function within each cell. Three types of interfaces between the *same* and *different* fluids can be recognized at a cell boundary, as seen in Fig. 3: the gas–gas ($\overline{ab}$ and $\overline{gh}$), liquid–liquid ($\overline{cd}$ and $\overline{ef}$), and gas–liquid interfaces ($\overline{bc}, \overline{cg}$ and $\overline{fg}$). Naturally, the numerical flux at the cell interface now comprises contributions from these interfaces. Thus, Eq. (5) can be expanded as follows:

$$\frac{\triangle x}{\triangle t}\delta_t \begin{pmatrix} \alpha_i\rho_i \\ \alpha_i\rho_i u_i \\ \alpha_i E_i \end{pmatrix}_j + \delta_x(\vartheta_{i-i}\mathbf{f}_{i-i} + \vartheta_{i'-i}\mathbf{f}_{i'-i} + \vartheta_{i-i'}\mathbf{f}_{i-i'}) + p_j \frac{\triangle x}{\triangle t}\begin{pmatrix} 0 \\ 0 \\ \delta_t\alpha_i \end{pmatrix}_j - p_j \begin{pmatrix} 0 \\ \delta_x^{\bigstar}\alpha_i \\ 0 \end{pmatrix} = 0. \tag{7}$$

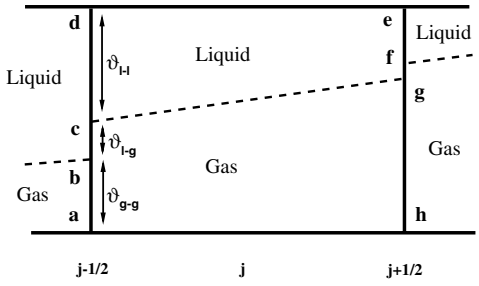

Fig. 3. Illustration of the one dimensional stratified flow.

The subscript i' denotes the phase being different from i, e.g., $i' = l$ when $i = g$. It is understood that the letter "j" is reserved for mesh indexing. Also, the numerical fluxes on the interfaces between the same fluids are denoted by $\mathbf{f}_{i-i}$ and the fluxes between different fluids denoted by $\mathbf{f}_{i-i'}$ and $\mathbf{f}_{i'-i}$. The functions, ϑ_{i-i}, $\vartheta_{i-i'}$ and $\vartheta_{i'-i}$, denote the effective lengthes of the interfaces at the cell boundary and they are defined as

$$\vartheta_{g-g} = \min((\alpha_g)_L, (\alpha_g)_R), \tag{8}$$

$$\vartheta_{l-l} = \min((\alpha_l)_L, (\alpha_l)_R), \tag{9}$$

$$\vartheta_{g-l} = \max(0, -\Delta\alpha_g) = \max(0, \Delta\alpha_l), \tag{10}$$

$$\vartheta_{l-g} = \max(0, -\Delta\alpha_l) = \max(0, \Delta\alpha_g), \tag{11}$$

where

$$\Delta(\cdot) = (\cdot)_R - (\cdot)_L, \tag{12}$$

where subscripts "L" and "R" refer to the "left" and "right" sides of the cell interface.

Then, it is easy to show the following identities:

$$\vartheta_{g-g} + \vartheta_{l-l} + \vartheta_{g-l} + \vartheta_{l-g} = 1, \tag{13}$$

$$\vartheta_{g-g} + \vartheta_{g-l} = (\alpha_g)_L, \tag{14}$$

$$\vartheta_{l-l} + \vartheta_{l-g} = (\alpha_l)_L, \tag{15}$$

and

$$\vartheta_{g-l} \cdot \vartheta_{l-g} = 0. \tag{16}$$

The notion of effective lengthes is new. Hence, further clarification is useful. For example, ϑ_{g-l} will represent the effective length of the gas–liquid interface with gas fluid on its left side (hence the left subscript) and liquid on the right side. The definition for ϑ_{l-g} is similar, but with liquid on the left and gas on the right.

For the pressure force at the in-cell interface, the last term in Eq. (5), a new spatial difference operator is warranted to reflect the fact that it is only applied to the portion *inside* the cell.

$$\delta_x^{\star}(\cdot) = (\cdot)_{j+1/2,L} - (\cdot)_{j-1/2,R}. \tag{17}$$

Noting that the difference operator in Eq. (12) is referred to the same cell interface, while $\delta_x^{\star}$ is referred to two different cell interfaces.

2.3. The AUSM$^+$-up method

The AUSM-family schemes have been developed over the years for single phase flows; they have been shown to possess several desirable properties which lead to a robust and accurate method for solving flows at all speeds, see [15,19,20] for details. Its algorithm is rather simple, yet its accuracy rivals that often associated with typical flux difference schemes, such as the Roe scheme and the Osher scheme. A unique feature of the AUSM schemes is that it can be readily applied to equations with complicated eigensystem, because it is not explicitly based on the structure of eigensystem. In this paper we shall extend the single phase version of the AUSM methods, specifically the one given in [19], to the multifluid system and demonstrate that the new method, AUSM$^+$-up, can provide accurate and stable results. In what follows, we will discuss the algorithm in details.

For a single fluid, the AUSM$^+$ scheme writes the interface flux $\mathbf{f}_{i-i}$ as a sum of convection flux $\mathbf{f}_{i-i}^c$ and pressure flux $\mathbf{f}_{i-i}^p$:

$$\mathbf{f}_{i-i} = \mathbf{f}_{i-i}^c + \mathbf{f}_{i-i}^p = \dot{m}_{i-i}\boldsymbol{\Psi}_{i,L/R} + \mathbf{p}_{i-i}, \tag{18}$$

in which the convected variables $\boldsymbol{\Psi} = (1, u, H)^T$ are evaluated by a simple upwind definition. That is, depending on the sign of the interface Mach number M_{i-i} (whose definition is to be defined later), we define, by using the notation "L/R",

$$\mathbf{\Psi}_{i,L/R} = \begin{cases} \mathbf{\Psi}_{\mathrm{L}} & \text{if} \quad M_{i-i} \geqslant 0, \\ \mathbf{\Psi}_{\mathrm{R}} & \text{otherwise.} \end{cases} \tag{19}$$

The definition of mass flux $\dot{m}_{i-i}$ and pressure flux $\mathbf{p}_{i-i} = (0, p_{i-i}, 0)^{\mathrm{T}}$ is central in the AUSM-family methods; hence, extra attention is required for the multifluid model, which will be described in detail below. First, the mass flux is further expressed as

$$\dot{m}_{i-i} = a_{i-i} M_{i-i} \rho_{i,\mathrm{L/R}}, \tag{20}$$

with

$$M_{i-i} = \mathscr{M}^{+}_{(4)}(M_{i,\mathrm{L}}) + \mathscr{M}^{-}_{(4)}(M_{i,\mathrm{R}}). \tag{21}$$

The Mach number at the "left" and "right" states are defined as

$$M_{i,\mathrm{L/R}} = \frac{u_{i,\mathrm{L/R}}}{a_{i-i}}, \tag{22}$$

where a_{i-i} is known as "numerical" speed of sound [16], whose specification is interesting because certain numerically advantageous features can be obtained by using different considerations. In other words, its specification is not unique, but it is nevertheless related to and on the order of the physical speed of sound. Based on our previous study of single phase flows [15], it is advantageous for calculating a moving discontinuity to use a common speed of sound at the cell interface. Here, we adopt the same idea by defining a common value for multifluid flows.

For the multifluid model, various choices for defining the speed of sound have appeared in the literature. We employ the numerical speed of sound a_{mix} derived for stratified (separated) flow, which is given by Wallis [21], also used in Hancox [22] and Toumi [23], based on a weighted harmonic mean of two quantities,

$$\frac{1}{a^2_{\mathrm{mix}}}\left(\frac{\alpha_{\mathrm{l}}}{\rho_{\mathrm{l}}} + \frac{\alpha_{\mathrm{g}}}{\rho_{\mathrm{g}}}\right) = \frac{\alpha_{\mathrm{l}}}{\rho_{\mathrm{l}} a^2_{\mathrm{l}}} + \frac{\alpha_{\mathrm{g}}}{\rho_{\mathrm{g}} a^2_{\mathrm{g}}}. \tag{23}$$

It is noted that a^2_{mix} lies between a^2_{g} and a^2_{l} and has the following limiting values: (1) $a^2_{\mathrm{mix}} = O(a^2_{\mathrm{g}})$ for $\alpha_{\mathrm{g/l}} = O(1)$, since $\rho_{\mathrm{l}} \gg \rho_{\mathrm{g}}$, and (2) $a^2_{\mathrm{mix}} \to O(a^2_{\mathrm{l/g}})$ when $\alpha_{\mathrm{g/l}} \to 0$, that is, when one fluid disappears, the speed of sound of the other fluid naturally assumes. This formula is different from the speed of sound appropriate for the homogeneous flow where only one set of equations is needed and its value can fall much below a_{g} and a_{l}, especially when $\alpha_{\mathrm{g}} = 0.5$. It is numerically preferable that the numerical speed of sound falls between the range of both individual fields in order to maintain smoothness of solution. By virtue of the above consideration, we now use Eq. (23) for the common speed of sound to define the Mach number for both fluids, i.e.,

$$a_{i-i} = a_{\mathrm{mix}}, \quad i = l \text{ or } g. \tag{24}$$

The polynomial functions in Eq. (21) are given as

$$\mathscr{M}^{\pm}_{(4)}(M) = \begin{cases} \mathscr{M}^{\pm}_{(1)} & \text{if } |M| \geqslant 1, \\ \mathscr{M}^{\pm}_{(2)}[1 \mp 2\mathscr{M}^{\mp}_{(2)}] & \text{otherwise.} \end{cases} \tag{25}$$

where

$$\mathscr{M}^{\pm}_{(1)} = \frac{1}{2}(M \pm |M|), \tag{26}$$

$$\mathscr{M}^{\pm}_{(2)} = \pm\frac{1}{4}(M \pm 1)^2. \tag{27}$$

Next, the interface pressure p_{i-i} is defined as

$$p_{i-i} = \mathscr{P}^{+}_{(5)}(M_{i,\mathrm{L}}) p_{\mathrm{L}} + \mathscr{P}^{-}_{(5)}(M_{i,\mathrm{R}}) p_{\mathrm{R}}. \tag{28}$$

Notice that we do not assign the phase index "i" to the pressure p_{L} or p_{R} because we assume a single pressure common to both phases in the two-fluid model under consideration. Similar to the Mach number polynomials, we also have the corresponding ones for pressure, but using the same set of basis polynomials,

$$\mathscr{P}^{\pm}_{(5)}(M) = \begin{cases} \frac{1}{M}\mathscr{M}^{\pm}_{(1)} & \text{if} \quad |M| \geqslant 1, \\ \mathscr{M}^{\pm}_{(2)}[\pm 2 - M \mp 3M\mathscr{M}^{\mp}_{(2)}] & \text{otherwise.} \end{cases} \tag{29}$$

Our previous work [8] shows that when the equations of state for water is used, both the AUSM$^+$ and AUSM$^+$-a [14] schemes generate numerical oscillations near discontinuities. To suppress these oscillations, we can add some properly-scaled dissipation terms to the AUSM$^+$ scheme to enhance the coupling between the mass flux (or convection terms) and pressure. We respectively introduce into the convection flux a dissipation term D_p based on pressure difference and into the pressure flux a dissipation term D_u based on velocity difference. The use of the dissipation terms based on velocity and pressure are originally proposed to solve low speed single phase flows [18–20]; they can effectively enhance the stability and convergence. Here, we rewrite the mass flow rate $\dot{m}_{i-i}$ and the interface pressure p_{i-i} in the following forms:

$$\dot{m}_{i-i} = \text{Eq. (20)} + D_{p_{i-i}}, \tag{30}$$

$$p_{i-i} = \text{Eq. (28)} + D_{ui-i}. \tag{31}$$

When dealing with the compressible liquid fluid, we adopt the same idea and make appropriate scaling adjustments to the dissipation terms. Formal derivation of the scaling of the dissipation terms can be found in [19]. Specifically, we write D_p and D_u as:

$$D_{p_{i-i}} = \kappa_p \frac{\Delta M_i \max(1 - \overline{M}_i^2, 0)(p_{\mathrm{L}} - p_{\mathrm{R}})}{\bar{a}_i}, \tag{32}$$

$$D_{ui-i} = \kappa_u \mathscr{P}^{+}_{(5)}(\overline{M}_i)\mathscr{P}^{-}_{(5)}(\overline{M}_i)\bar{\rho}_i\bar{a}_i(u_{i,\mathrm{L}} - u_{i,\mathrm{R}}), \tag{33}$$

where

$$\Delta M_i = \mathscr{M}^{+}_{(4)}(M_{i,\mathrm{L}}) - \mathscr{M}^{+}_{(1)}(M_{i,\mathrm{L}}) - \mathscr{M}^{-}_{(4)}(M_{i,\mathrm{R}}) + \mathscr{M}^{-}_{(1)}(M_{i,\mathrm{R}}).$$

The parameters $\bar{a}_i$ and $\overline{M}_i$ here are obtained with the arithmetic mean of the "L" and "R" states, i.e. $\bar{a}_i = (a_{i,\mathrm{L}} + a_{i,\mathrm{R}})/2$. In this paper, the AUSM$^+$-up scheme is uniformly applied to gas–gas and liquid–liquid interface. And the coefficients $\kappa_p = \kappa_u = 1$ are used for all the test problems, unless they are noted otherwise, e.g. $\kappa_p = \kappa_u = 0$.

2.4. Exact Riemann solver for gas–liquid interface

As noted above, we use AUSM$^+$-up scheme to calculate the numerical flux between the same fluid, $\mathbf{f}_{\mathrm{g\text{–}g}}$ and $\mathbf{f}_{\mathrm{l\text{–}l}}$. What remains to be done is the evaluation of numerical flux between different fluids, $\mathbf{f}_{\mathrm{g\text{–}l}}$ and $\mathbf{f}_{\mathrm{l\text{–}g}}$. To our knowledge, no exact Riemann solver is known in the literature for numerical flux of a general two-fluid model of a real fluid. Fortunately, because the stiffened gas EOS is only slightly different from the ideal gas EOS, an exact form of the Riemann solution is possible, requiring a small numerical iteration for solving pressure. It involves exactly the same procedure as in the ideal gas case. Since there is still an algebraic difference from that of ideal gas, it is instructive to show the derivation of the exact Riemann solution. Its details are given in Appendix B for the interested reader[3].

Since the exact Riemann solver is still more expensive to compute than other approximate solvers, we shall only use the exact Riemann solver in the vicinity of the fluid interface. More specifically, we use the exact Riemann solver to calculate $\mathbf{f}_{i-i'}$ in Eq. (7) when $\vartheta_{i-i'} > 5\epsilon$, where ϵ is used to define the minimum value of α_i and, generally, we have $\epsilon = 10^{-6} \sim 10^{-8}$ in our computation. Otherwise, we just use the simple upwind scheme to calculate the convection flux and use the central difference scheme to calculate the pressure flux.

Referring to Appendix B, the fluid velocity in the transition region $u^{\bigstar}$ can be calculated by Eq. (B.3) or (B.5). The numerical fluxes across the inter-phasic interface depend on the relative position of fluids and the direction of the cell boundary. Considering the situation where $(\alpha_{\mathrm{g}})_{\mathrm{L}} > (\alpha_{\mathrm{g}})_{\mathrm{R}}$, hence $\vartheta_{\mathrm{g\text{–}l}} > 0$ and $\vartheta_{\mathrm{l\text{–}g}} = 0$. Then for the left cell $(j-1)$, the numerical flux on the cell boundary is

[3] One of the reviewers points out that the exact Riemann solver was given for the stiffened gas in [24], which we were not aware of. Since this work is written in Russian and no English translation of it is available, we include its derivation in Appendix B for completeness.

$$\mathbf{f}_{g\text{–}l} = \begin{Bmatrix} \max(0,u^\star)(\rho_g^\star)_L \\ \max(0,u^\star)(\rho_g^\star)_L u^\star \\ \max(0,u^\star)((\rho_g^\star)_L (E_g^\star)_L + p^\star) \\ \min(0,u^\star)(\rho_l^\star)_R \\ \min(0,u^\star)(\rho_l^\star)_R u^\star \\ \min(0,u^\star)((\rho_l^\star)_R (E_l^\star)_R + p^\star) \end{Bmatrix} + \begin{Bmatrix} 0 \\ p^\star \\ 0 \\ 0 \\ 0 \\ 0 \end{Bmatrix}. \tag{34}$$

And for the right cell (j), the numerical flux is

$$\mathbf{f}_{g\text{–}l} = \begin{Bmatrix} \max(0,u^\star)(\rho_g^\star)_L \\ \max(0,u^\star)(\rho_g^\star)_L u^\star \\ \max(0,u^\star)((\rho_g^\star)_L (E_g^\star)_L + p^\star) \\ \min(0,u^\star)(\rho_l^\star)_R \\ \min(0,u^\star)(\rho_l^\star)_R u^\star \\ \min(0,u^\star)((\rho_l^\star)_R (E_l^\star)_R + p^\star) \end{Bmatrix} + \begin{Bmatrix} 0 \\ 0 \\ 0 \\ 0 \\ p^\star \\ 0 \end{Bmatrix}, \tag{35}$$

where the first and second terms in the RHS of above equations represent the convection flux and pressure flux respectively. It should be noted that the pressure in the momentum equation is applied to the gas fluid in the left cell and liquid fluid in the right cell. This is the inter-phasic interaction across the cell boundary, which makes our method different from others.

We remark that recognizing the use of flux contributions between unlike phases, $\mathbf{f}_{g\text{–}l}$ and $\mathbf{f}_{l\text{–}g}$, is essential in the present formulation. However, the numerical representation of these fluxes is open to different ideas, as in the development of single fluid numerical fluxes; using the exact Riemann solver appears to be a safe route since we did not know anything better than it. As will be discussed later in Section 3.4, the substitute of our previous rough approximation [8] with the current one has yielded improvements in accuracy and robustness. On the other hand, there are disadvantages with using the exact Riemann solver, especially in the case of general fluids having a complex equation of state, thus preventing from obtaining an analytical equation to solve for $p^\star$. It is likely that one can develop other robust and accurate ways of dealing with the fluxes between mixed fluids. A research in this direction will be very desirable since it is general and the one for single fluid is just its special case.

2.5. Summary of the numerical fluxes for the multifluid model

In summary, we can give the numerical fluxes in Eq. (7) in a general form. For simplicity, we shall interchangeably use the following subscripts: $1/2 \equiv j + 1/2$, and $-1/2 \equiv j - 1/2$. Then $\mathbf{f}_{i,\pm 1/2}$ denotes the numerical fluxes of fluid i at the cell boundaries $j \pm 1/2$ of cell j. Substituting the component fluxes developed above, we have the numerical flux in Eq. (7) expanded as

$$\begin{aligned} \mathbf{f}_{i,1/2} &= [\vartheta_{i-i}\mathbf{f}_{i-i} + \vartheta_{i-i'}\mathbf{f}_{i-i'} + \vartheta_{i'-i}\mathbf{f}_{i'-i}]_{1/2} \\ &= \vartheta_{i-i,1/2}[(a_{i-i}M_{i-i}\rho_{i,L/R} + D_{p_{i-i}})\Psi_{i,L/R} + (0,p_{i-i},0)^{\mathrm{T}}]_{1/2} + \vartheta_{i-i',1/2}[\max(0,u^\star)\rho_i^\star\Psi_i^\star \\ &\quad + (0,p^\star,0)^{\mathrm{T}}]_{1/2} + \vartheta_{i'-i,1/2}\min(0,u^\star)(\rho_i^\star\Psi_i^\star)_{1/2}, \end{aligned} \tag{36}$$

where

$$p_{i-i,1/2} = [\mathscr{P}^+_{(5)}(M_{i,L})p_{i,L} + \mathscr{P}^-_{(5)}(M_{i,R})p_{i,R} + D_{ui-i}]_{1/2}.$$

And the numerical flux $\mathbf{f}_{i,-1/2}$ for cell j is

$$\begin{aligned} \mathbf{f}_{i,-1/2} &= \vartheta_{i-i,-1/2}[(a_{i-i}M_{i-i}\rho_{i,L/R} + D_{p_{i-i}})\Psi_{i,L/R} + (0,p_{i-i},0)^{\mathrm{T}}]_{-1/2} + \vartheta_{i-i',-1/2}\max(0,u^\star)(\rho_i^\star\Psi_i^\star)_{-1/2} \\ &\quad + \vartheta_{i'-i,-1/2}[\min(0,u^\star)\rho_i^\star\Psi_i^\star + (0,p^\star,0)^{\mathrm{T}}]_{-1/2}. \end{aligned} \tag{37}$$

A benefit of using the stratified flow method is that it automatically meets the pressure non-disturbing condition described in Introduction. To show this, we consider the case of a moving contact discontinuity across which velocity and pressure are continuous, i.e., $p_L = p_R = p$ and $u_L = u_R = u$. Hence it is easy to show

$$p_{\pm 1/2,L/R} = p_{i-i_{,\pm 1/2}} = p^{\star}_{\pm 1/2} = p, \tag{38}$$

and

$$u_{\pm 1/2,L/R} = (a_i M_i)_{\pm 1/2} = u^{\star}_{\pm 1/2} = u. \tag{39}$$

First, referring to Eqs. (7), (36) and (37), we collect all the pressure terms in the momentum equation and denote it as Γ_m:

$$\Gamma_m = [\vartheta_{i-i} p_{i-i} + \vartheta_{i-i'} p^{\star}]_{1/2} - [\vartheta_{i-i} p_{i-i} + \vartheta_{i'-i} p^{\star}]_{-1/2} - p_j \delta^{\star}_x \alpha_i. \tag{40}$$

Since

$$\begin{aligned} &[\vartheta_{i-i} + \vartheta_{i-i'}]_{1/2} = (\alpha_i)_{1/2,L}, \\ &[\vartheta_{i-i} + \vartheta_{i'-i}]_{-1/2} = (\alpha_i)_{-1/2,R}. \\ &\delta^{\star}_x(\cdot) = (\cdot)_{1/2,L} - (\cdot)_{-1/2,R}. \end{aligned} \tag{41}$$

Then, Eq. (40) simplifies to

$$\Gamma_m = p[\vartheta_{i-i} + \vartheta_{i-i'}]_{1/2} - p[\vartheta_{i-i} + \vartheta_{i-i'}]_{-1/2} - p\delta^{\star}_x \alpha_i = 0. \tag{42}$$

Similarly in the energy equation, we can also collect all the pressure terms and denote it by Γ_E:

$$\begin{aligned} \Gamma_E = {} & p\frac{\triangle x}{\triangle t}\delta_t \alpha_j + [\vartheta_{i-i} a_i M_i p_{L/R} + \vartheta_{i-i'} \max(0, u^{\star}) p^{\star} + \vartheta_{i'-i} \min(0, u^{\star}) p^{\star}]_{1/2} \\ & - [\vartheta_{i-i} a_i M_i p_{L/R} + \vartheta_{i-i'} \max(0, u^{\star}) p^{\star} + \vartheta_{i'-i} \min(0, u^{\star}) p^{\star}]_{-1/2}. \end{aligned} \tag{43}$$

It is further reduced to

$$\Gamma_E = p\frac{\triangle x}{\triangle t}\delta_t \alpha_j + p[\vartheta_{i-i} u + \vartheta_{i-i'} \max(0,u) + \vartheta_{i'-i} \min(0,u)]_{1/2} - p[\vartheta_{i-i} u + \vartheta_{i-i'} \max(0,u) + \vartheta_{i'-i} \min(0,u)]_{-1/2}. \tag{44}$$

If $u \geqslant 0$, we get

$$\Gamma_E = p\left(\frac{\triangle x}{\triangle t}\delta_t \alpha_j + u[(\alpha_i)_{1/2,L} - (\alpha_i)_{-1/2,L}]\right) = 0, \tag{45}$$

by virtue of the discrete form of the transport equation of volume fraction function. For $u_j < 0$, we also have

$$\Gamma_E = p\left(\frac{\triangle x}{\triangle t}\delta_t \alpha_j + u[(\alpha_i)_{1/2,R} - (\alpha_i)_{-1/2,R}]\right) = 0. \tag{46}$$

Consequently, all the terms involved with pressure are summed up to zero, the system is left with convective fluxes only, which are convected with the constant speed u. Thus, the pressure non-disturbing condition is met and the stratified flow model can capture a stationary contact discontinuity exactly.

2.6. Multi-dimensional extension

To extend the above 1D method to higher dimension, we first write the general version of Eq. (4) as

$$\frac{\partial}{\partial t}\int_V \begin{pmatrix} \alpha_i \rho_i \\ \alpha_i \rho_i \vec{\mathbf{v}}_i \\ \alpha_i \rho_i E_i \end{pmatrix} \mathrm{d}V + \oint (\alpha_i \mathbf{f}_i)\, \mathrm{d}S + \frac{\partial}{\partial t}\int_V p \begin{pmatrix} 0 \\ 0 \\ \alpha_i \end{pmatrix} \mathrm{d}V - \int_V p \begin{pmatrix} 0 \\ \nabla \alpha_i \\ 0 \end{pmatrix} \mathrm{d}V = 0. \tag{47}$$

After discretization performed as before, the above equation becomes

$$\frac{V_j}{\triangle t}\delta_t\begin{pmatrix}\alpha_i\rho_i\\ \alpha_i\rho_i\vec{\mathbf{v}}_i\\ \alpha_i\rho_i E_i\end{pmatrix}_j+\sum_{l=1}^{m}(\alpha_i\mathbf{f}_i)_l S_l+p_j\frac{V_j}{\triangle t}\begin{pmatrix}0\\ 0\\ \delta_t\alpha_i\end{pmatrix}_j-p_j\sum_{l=1}^{m}\begin{pmatrix}0\\ \alpha_{i,\mathrm{L}}\vec{\mathbf{n}}\\ 0\end{pmatrix}_l S_l=0, \tag{48}$$

with

$$\alpha_i\mathbf{f}_i=(\vartheta_{i-i}\mathbf{f}_{i-i}+\vartheta_{i'-i}\mathbf{f}_{i'-i}+\vartheta_{i-i'}\mathbf{f}_{i-i'}). \tag{49}$$

Here m is the number of cell faces enclosing cell j. All of the cell faces are defined to be directed outward from the cell and $\alpha_{i,\mathrm{L}}$ is the reconstructed void function located just at the inner side of cell faces.

2.7. Interfacial pressure correction term

It is well known that the system of inviscid multifluid equations, Eq. (1), is non-hyperbolic. To make the system hyperbolic, thus well-posed, an interfacial pressure correction term in the form of first spatial derivative can be added in order to alter the characteristics of the system. Hence, the original multifluid model of Eq. (1), enhanced with the pressure correction, p^{int}, now appears as

$$\begin{aligned}&\frac{\partial(\alpha_i\rho_i)}{\partial t}+\nabla\cdot(\alpha_i\rho_i\vec{\mathbf{v}}_i)=0,\\ &\frac{\partial(\alpha_i\rho_i\vec{\mathbf{v}}_i)}{\partial t}+\nabla\cdot(\alpha_i\rho_i\vec{\mathbf{v}}_i\vec{\mathbf{v}}_i)+\nabla(\alpha_i p)=(p-p^{\mathrm{int}})\nabla\alpha_i,\\ &\frac{\partial(\alpha_i\rho_i E_i)}{\partial t}+\nabla\cdot(\alpha_i\rho_i H_i\vec{\mathbf{v}}_i)=-(p-p^{\mathrm{int}})\frac{\partial\alpha_i}{\partial t}.\end{aligned} \tag{50}$$

The pressure correction term we adopt is the one first proposed by Stuhmiller [5],

$$p^{\mathrm{int}}=\sigma\frac{\alpha_{\mathrm{g}}\rho_{\mathrm{g}}\alpha_{\mathrm{l}}\rho_{\mathrm{l}}}{\alpha_{\mathrm{g}}\rho_{\mathrm{l}}+\alpha_{\mathrm{l}}\rho_{\mathrm{g}}}|\vec{\mathbf{v}}_{\mathrm{g}}-\vec{\mathbf{v}}_{\mathrm{l}}|^2. \tag{51}$$

where σ is a parameter and the system becomes hyperbolic if

$$\sigma\geqslant 1, \tag{52}$$

under the low relative Mach number condition of $|\vec{\mathbf{v}}_{\mathrm{g}}-\vec{\mathbf{v}}_{\mathrm{l}}|\ll a_{\mathrm{g}}$. Unfortunately this condition is shown recently in [25] to be insufficient to guarantee hyperbolicity if the relative Mach number is finite, it requires a much larger value than unity, depending on the flow conditions and α_i. The effect of σ on the solution will be addressed in detail in the Ransom's faucet problem in Section 3.2.

Here we adopt the idea of pressure correction into our framework of stratified fluid and introduce pressure correction p_{int} into Eq. (48). As described above, the stratified fluid model suggests two types of inter-phasic fluxes – one is within the same cell and the other between neighboring cells. Recognizing this difference makes it quite clear as to how the interfacial pressure correction term should be implemented in the discretized equation, specifically with respect to the second, third, and fourth terms in Eq. (48). That is to say, only those pressure fluxes that envisage interactions between different fluids need be implemented with the pressure correction. Hence, Eq. (48) becomes

$$\begin{aligned}&\frac{V_j}{\Delta t}\delta_t\begin{pmatrix}\alpha_i\rho_i\\ \alpha_i\rho_i\vec{\mathbf{v}}_i\\ \alpha_i E_i\end{pmatrix}+\sum_{l=1}^{m}[\vartheta_{i-i}\mathbf{f}_{i-i}+\vartheta_{i-i'}(\mathbf{f}_{i-i'}-\mathbf{p}^{\mathrm{int}}_{i-i'})+\vartheta_{i'-i}(\mathbf{f}_{i'-i}-\mathbf{p}^{\mathrm{int}}_{i'-i})]_l S_l\\ &\quad+(p_j-p_j^{\mathrm{int}})\frac{V_j}{\Delta t}\begin{pmatrix}0\\ 0\\ \delta_t\alpha_i\end{pmatrix}-(p_j-p_j^{\mathrm{int}})\sum_{l=1}^{m}\begin{pmatrix}0\\ \alpha_{i,\mathrm{L}}\vec{\mathbf{n}}\\ 0\end{pmatrix}_l S_l=0.\end{aligned} \tag{53}$$

The interfacial pressure correction is seen to appear in two places, respectively as p_j^{int} (which is simply Eq. (51) evaluated at "j") for the interface within the cell and $\mathbf{p}_{i-i'}^{\text{int}}$ between the cells, which is given as follows.

$$\mathbf{p}_{i-i'}^{\text{int}} = p_{i-i'}^{\text{int}}(0, \vec{\mathbf{n}}, 0)^{\mathrm{T}}, \tag{54}$$

where

$$p_{i-i'}^{\text{int}} = \sigma \frac{\hat{\alpha}_i \hat{\alpha}_{i'} (\rho_i)_j (\rho_{i'})_{j'}}{\hat{\alpha}_i (\rho_{i'})_{j'} + \hat{\alpha}_{i'} (\rho_i)_j} |(\vec{\mathbf{v}}_i)_j - (\vec{\mathbf{v}}_{i'})_{j'}|^2, \tag{55}$$

and

$$\hat{\alpha}_i = \frac{1}{2}((\alpha_i)_j + (\alpha_i)_{j'}) = 1 - \hat{\alpha}_{i'}. \tag{56}$$

In the above equations, we use the subscript j' to denote the cell that neighbors cell j through the cell boundary l.

The introduction of the interfacial pressure correction p^{int} is to improve the stability of the system, and it should not be too large to change the physics of the flow. In most of our test problems, p^{int} is much smaller than the local pressure p_j in the flow. However, under some extreme conditions it is possible that p^{int} is larger than the surrounding pressures, thereby resulting in a significant departure from the original problem. Hence, an additional limit on the pressure correction terms is imposed.

$$p_j^{\text{int}} = \min(p_j^{\text{int}}, \varepsilon_p p_j), \tag{57}$$

and

$$p_{i-i'}^{\text{int}} = \min(p_{i-i'}^{\text{int}}, \varepsilon_p \min(p_j, p_{j'})). \tag{58}$$

In our practice, we usually set $\varepsilon_p = 10^{-2} \sim 10^{-3}$, which has been found sufficient to keep the simulation well-behaved[4]. Several runs were conducted to investigate the effects on the solution due to ε_p for some computationally-challenging problems, e.g., shock-droplet problem in Section 3.5; no noticeable effects were found for it varying from 0.001 to 0.1.

2.8. Time integration method and updating of variables

A multi-step Runge–Kutta method is used for advancing the solution in time and we will omit its description since it is rather standard. However, unlike the single fluid ideal gas flow, the updating of variables at the new time level for multifluid equations gives rise to a new problem requiring additional care. Below describes the procedure used in this study. For two dimensional flow, the time discretization of Eq. (53) may be written as:

$$\begin{pmatrix} \mathscr{W}_i \\ \mathscr{M}_i \\ \mathscr{N}_i \\ \mathscr{E}_i \end{pmatrix} = \begin{pmatrix} \alpha_i^s \rho_i^s \\ \alpha_i^s \rho_i^s u_i^s \\ \alpha_i^s \rho_i^s v_i^s \\ \alpha_i^s \rho_i^s E_i^s + (p^n - p_j^{\text{int}})\alpha_i^s \end{pmatrix} = \begin{pmatrix} \alpha_i^n \rho_i^n \\ \alpha_i^n \rho_i^n u_i^n \\ \alpha_i^n \rho_i^n v_i^n \\ \alpha_i^n \rho_i^n E_i^n + (p^n - p_j^{\text{int}})\alpha_i^n \end{pmatrix} - \omega \frac{\Delta t}{V} \mathbf{R}_i, \tag{59}$$

where $\mathbf{R}_i$ is the summation of the second and fourth terms in Eq. (53). The superscripts n and s are the indices for the present and next time steps respectively, and ω is the parameter used for each sub-step of the Runge–Kutta method. To calculate the primitive variables at the next time step, the EOS of fluids must be applied to

[4] The physical meaning of the interfacial pressure is still debated every now and then and the correctness of the form, aside from rudimentary arguments, is far from resolved. Hence, it is argued here that this additive term must be small compared to the surrounding pressure (which is physical) so that the physical problem at hand is not significantly altered and yet it is sufficiently large to maintain the solution well behaved (a manifestation of hyperbolicity).

the above equation to update the pressure via an algebraic equation: a quadratic equation in the case of using the stiffened gas model,

$$(p^s)^2 + (-A + B + D)p^s - AC + BD = 0, \tag{60}$$

where

$$\begin{aligned} A &= (\gamma_g - 1)(\mathscr{E}_g - \Theta_g), \\ B &= -(\gamma_l - 1)(\mathscr{E}_l - \Theta_l - p^n) + \gamma_l p_\infty, \\ C &= \gamma_l p_\infty + (\gamma_l - 1)(p^n - p_j^{\text{int}}), \\ D &= (\gamma_g - 1)(p^n - p_j^{\text{int}}), \end{aligned}$$

and

$$\Theta_i = \frac{\mathscr{M}_i^2 + \mathscr{N}_i^2}{2\mathscr{W}_i}.$$

The pressure p^s is the positive root of the above equation. Then the other primitive variables can be derived easily,

$$\begin{aligned} &\alpha_g^s = \frac{\mathscr{E}_g - \Theta_g}{\frac{p^s}{\gamma_g - 1} + (p^n - p_j^{\text{int}})}, \quad \alpha_l^s = 1 - \alpha_g^s, \\ &u_i^s = \frac{\mathscr{M}_i}{\mathscr{W}_i}, \quad v_i^s = \frac{\mathscr{N}_i}{\mathscr{W}_i}, \quad e_i^s = \frac{1}{\mathscr{W}_i}(\mathscr{E}_i - \alpha_i^s(p^n - p_j^{\text{int}})) - \frac{1}{2}((u_i^s)^2 + (v_i^s)^2), \\ &T_g^s = \frac{(\gamma_g - 1)e_g^s}{R_g}, \quad T_l^s = \frac{\gamma_l e_l^s (p^s + p_\infty)}{(C_p)_l (p^s + \gamma_l p_\infty)}. \end{aligned}$$

Notice that the coefficients in Eq. (60) differ enormously, at least on the order of p_∞ of the liquid. The ratio between the largest and smallest coefficient might be as large as 10^{18} in some of our test cases, resulting in a large numerical error in solving p^s and α_g^s, even when double precision is used in the calculation. Hence, an additional Newton iteration method is used to improve the accuracy. From the energy equation of both fluids in Eq. (59), p^s and α_g^s are solved from the following equations simultaneously.

$$F_g = \alpha_g^s \left(\frac{p^s}{\gamma_g - 1} + (p^n - p_j^{\text{int}}) \right) + \Theta_g^s - \mathscr{E}_g^s = 0, \tag{61}$$

$$F_l = (1 - \alpha_g^s) \left(\frac{p^s + \gamma_l p_\infty}{\gamma_l - 1} + (p^n - p_j^{\text{int}}) \right) + \Theta_l^s - \mathscr{E}_l^s = 0. \tag{62}$$

Here $\Theta_{l/g}^s$ and $\mathscr{E}_{l/g}^s$ are the known quantities from the current updates of conservative variables as given in Eq. (59). To obtain (α_g^s, p^s), the above two equations are solved simultaneously via the Newton iteration method with the analytical solution of Eq. (60) as the initial guess. Generally, we can drive the functions, F_g and F_l, from $O(10^3)$ to $O(10^{-5})$ within 20 iterations. We emphasize that this additional step is required to ensure the decoding is precise, free of roundoff errors; it is performed at each time step before continuing on to the new time step. It should not be confused with the pressure relaxation used in [10] because this iterative procedure is merely an attempt to get numerically consistent solutions to Eqs. (61) and (62) before continuing on to the next time step. More discussion of this procedure is given in [8].

Another concern when solving Eq. (53) is that the numerical error of variables may be amplified when one of the phase is disappearing (or similarly appearing in full), i.e., α_g or $\alpha_l \to 0$. In this case, although the amount of the fluid is near void and its contributions to the flow field is essentially negligible, the calculation however can still become unstable if any variable associated to this fluid diverges. To control the numerical error (numerical instability) when one phase of fluid vanishes, we adopt the idea suggested in Paillère et al. [26], in which the fluids assume equilibrium immediately by mixing (blending) fluid states. For example, if α_g^s, which is obtained after the time integration, approaches zero and falls in the range $\epsilon_{\min} \leqslant \alpha_g^s \leqslant \epsilon_{\max}$, then we re-set the velocity and temperature fields of the disappearing phase by blending,

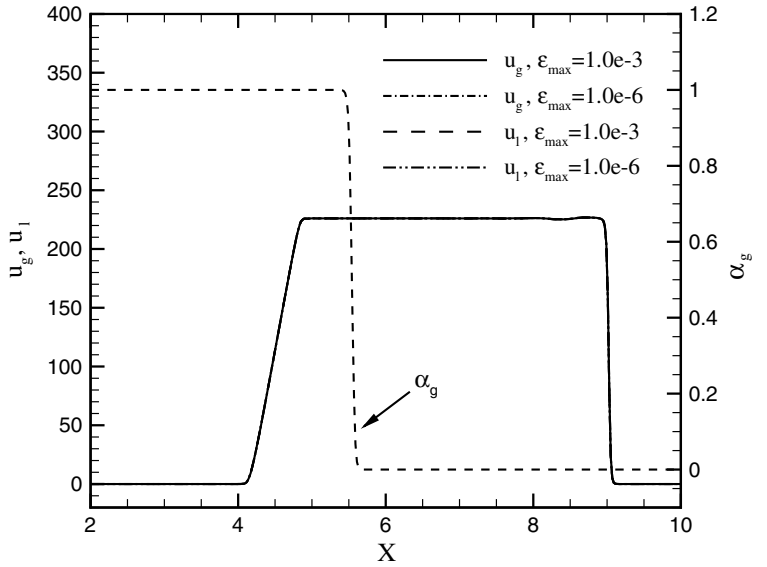

Fig. 4. Effect of ϵ_{max} on the solution of air–water shock tube problem (see Section 3.3); $\epsilon_{min} = 10^{-7}$.

$$(q_g^s)_{adjust} = G(\xi_g)q_g^s + (1 - G(\xi_g))q_l^s, \quad q = u, T \tag{63}$$

The function $G(\xi), \xi \in [0,1]$, is a smooth cubic polynomial interpolation with the properties: $G(0) = 0$, $G(1) = 1$ and $G'(0) = G'(1) = 0$. One easily finds the choice,

$$G(\xi) = -\xi^2(2\xi - 3),$$

where the normalized parameter is defined as

$$\xi = \frac{\alpha - \epsilon_{min}}{\epsilon_{max} - \epsilon_{min}}.$$

In these equations, $\epsilon_{min} > 0$ is a very small value defined by the lowest limit of $\alpha_i, i = g, l$, e.g., $\epsilon_{min} = \min(\alpha_g, 1 - \alpha_g)$ in the problem or a pre-set value ($10^{-6} \sim 10^{-7}$ in this paper), whichever is smaller; we chose $\epsilon_{max} = 10\epsilon_{min} \sim 100\epsilon_{max}$ in our calculations.

We present in Fig. 4 the effect on the solution of the air–water shock tube (see Section 3.3 for details) by varying the value of ϵ_{max} in a wide range, $10^{-3} \leqslant \epsilon_{max} \leqslant 10^{-6}$, while ϵ_{min} is set to be the same as $(\alpha_g)_{min} = 10^{-7}$. In the figure, the solutions using $\epsilon_{max} = 10^{-3}$ and 10^{-6} are indistinguishable (maximum difference in $|u_g - u_l|$ is 0.05 m/s). It confirms that the solutions are convergent and the present method is robust and accurate to handle the situation of phase disappearing/re-appearing.

3. Results and discussion

The 4-stage Runge–Kutta method is used for the time integration. The Osher–Chakravarthy TVD scheme [27] is chosen to provide third-order spatial accuracy for all results presented in this section, unless noted otherwise.

Several one and two dimensional test problems are used to study the capability of our method. We apply the new method described above to simulate several 1D multiphase problem, such as the Ransom's faucet problem and air–water shock tube problems. Then, two dimensional problems will be presented, including the shock–droplet interactions, underwater explosion, and underwater shock–bubble interactions.

For ease of referencing, we list in Table 1 the parameters relevant to the computation of each problem in this paper. The interfacial pressure constant is set to 2 throughout, except in the Ransom's faucet problem where a range of values are tested to show its effect on the solution. The CFL number is set to 0.5 for all cases except in the case of shock and water column(s) interaction for which a smaller value of 0.3 is used to maintain

Table 1
Parameters used in computed problems

Problem	σ	CFL	$(\kappa_p)_g$	$(\kappa_u)_g$	$(\kappa_p)_l$	$(\kappa_u)_l$	ε_p
Moving contact	2	0.5	0/1	0/1	0/1	0/1	10^{-2}
Ransom's Faucet	2	0.5	0/1	0/1	0/1	0/1	10^{-2}
Air–water shock tube	2	0.5	1	1	1	1	10^{-2}
Water–air shock tube	2	0.5	1	1	1	1	10^{-2}
Shock and water column	2	0.3	0	0	1	1	10^{-2}
Shock and bubble	2	0.5	0	0	1	1	10^{-2}
Underwater explosion	2	0.5	1	1	1	1	10^{-2}

See Eq. (51) for σ, (32) and (33) for (κ_p, κ_u), and (57) for ε_p. For the cases of the first two rows, 0/1 denotes that both values were used, resulting in no visible differences in the solutions.

stability. The diffusion terms $D_p(\kappa_p)$ and $D_u(\kappa_u)$ in Eqs. (32) and (33), used in the mass and pressure fluxes, are used in most cases. For the moving discontinuity problem and faucet problem, we do not use these diffusion terms since the pressure is basically constant throughout the computation domain. We also turn off these terms in the gas fluxes in the shock–water column and shock–bubble problems.

Unless stated otherwise, all variables are presented in the SI units, e.g., u in [m/s], T in [K], and p in Pa.

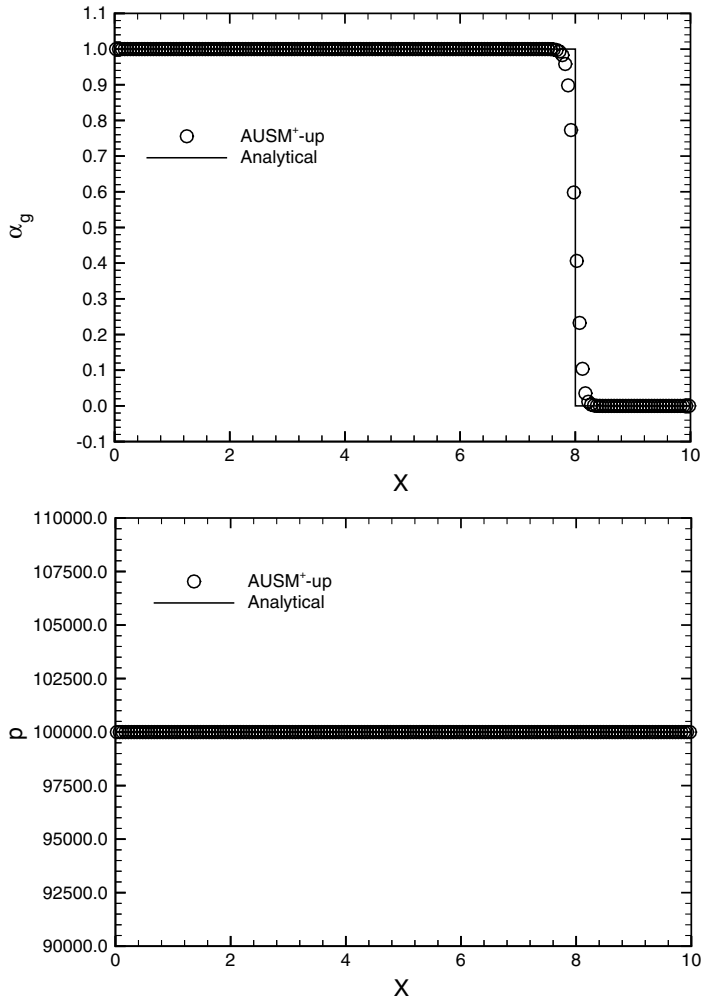

Fig. 5. Void fraction and pressure profiles of a moving discontinuity problem at time $t = 0.03$ s, 200 cells.

3.1. The moving discontinuity problem

We first applied our method to the moving contact discontinuity problem as a basic test. To accurately capture the moving discontinuity a numerical scheme is required to keep the positivity of the void fraction function and the uniformity of the pressure field as the flow continues. We set the initially condition as

$$(p, \alpha_g, u_i, T_i)_L = (10^5 \text{ Pa}, 1.0 - \epsilon, 100.0 \text{ m/s}, 300.0 \text{ K}),$$
$$(p, \alpha_g, u_i, T_i)_R = (10^5 \text{ Pa}, \epsilon, 100.0 \text{ m/s}, 300.0 \text{ K}),$$

where $\epsilon = 1.0 \times 10^{-8}$. A mesh of 200 cells was used for the computation. For this problem and the Ransom's faucet problem, we use $\kappa_p = \kappa_u = 0$, as there is no sharp pressure gradient in the flow.

The result at time $t = 0.03$ s is presented in Fig. 5. The proposed method is able to capture the contact discontinuity accurately without inflicting any disturbance in the pressure field, confirming that the pressure non-disturbance condition is satisfied and is consistent with the analysis given in Section 2.5.

3.2. Ransom's faucet problem

Referring to Fig. 6, the faucet problem introduced by Ransom [28] consists of air and a water jet confined in a channel, with the flow configurations at three time instants depicted. In the beginning, both the water column and the surrounding air are moving at a constant speed of 10 m/s. Then the gravity force is applied to the fluid, causing the water column to accelerate and get narrower so that the mass conservation is met. This is accompanied with a void wave moving toward the outlet. Finally, the flow becomes steady when its wavefront moves out of the computational domain. An analytical solution can be derived by assuming that the water is incompressible and the effect of air negligible.

We set up the inflow boundary condition as: the void fraction of air $\alpha_g = 0.2$, the velocities of both air and water $u_g = u_l = 10$ m/s, the temperatures $T_g = T_l = 300$ K, and the pressure is extrapolated from the interior point. At the outflow boundary, we set the pressure $p = 10^5$ Pa, and all the other primitive variables are extrapolated from inside. A mesh of 500 cells was used for the computation.

Fig. 7 shows the time evolution of the void fraction profile. The computed result compares well with the analytical solution and there are no oscillations in the result. It should be noted that most of the published results show a severe overshoot in void fraction profile behind the advancing wavefront. It is noted that

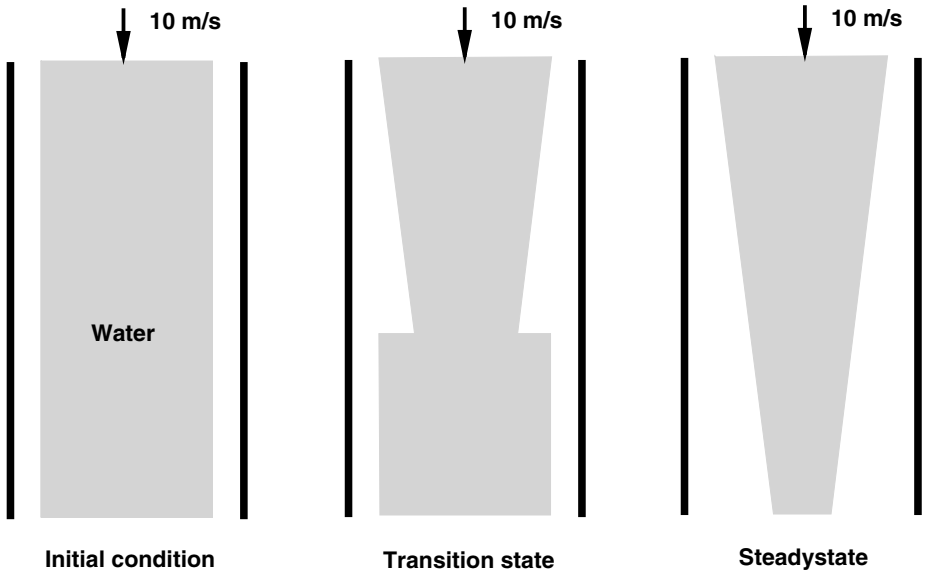

Fig. 6. Illustration of Ransom's water faucet problem.

any numerical scheme that does not satisfy the pressure non-disturbing condition will generate instability in the region where $\nabla\alpha_i \neq 0$, i.e., in the vicinity of fluid interface. This test demonstrates that the present method automatically satisfies the pressure non-disturbance condition at the discrete level and is able to enhance the stability of simulation.

Fig. 8 demonstrates how the interfacial pressure correction p^{int} influences the simulation result. Void fraction profiles calculated by different σ are shown. When $\sigma = 0$, the multifluid model is non-hyperbolic and ill-posed mathematically. Although the wavefront is sharply captured, there is still a minor glitch in the profile.

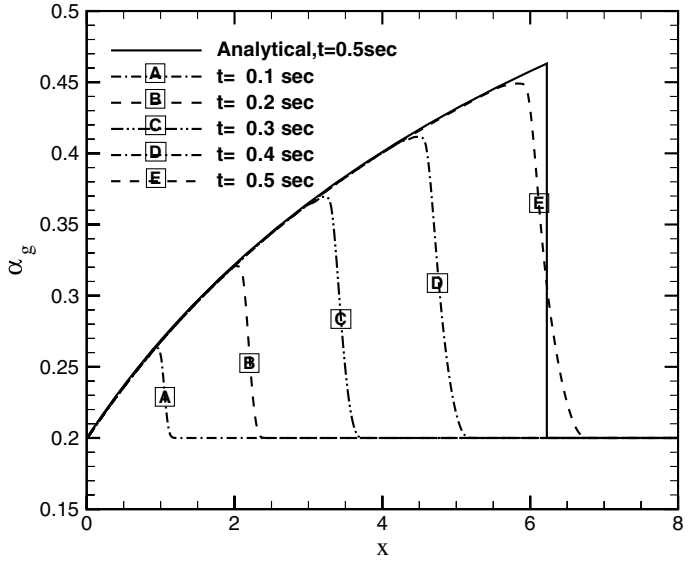

Fig. 7. Time evolution of the void fraction profile in the water faucet problem.

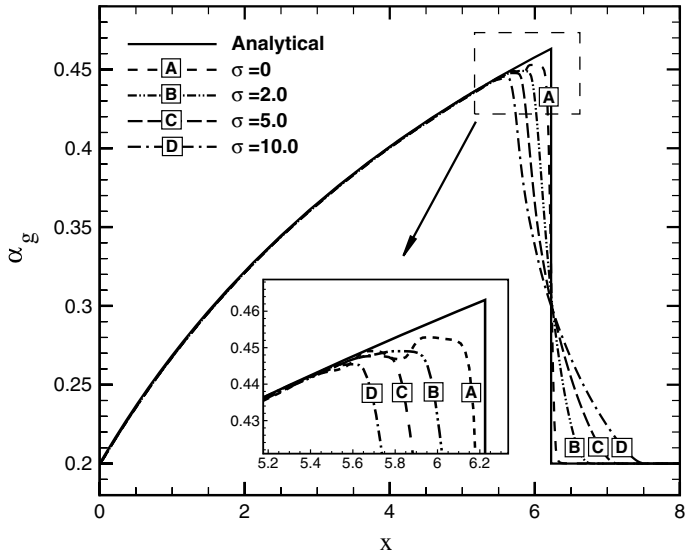

Fig. 8. The void fraction profiles based on different σ in the water faucet problem at time $t = 0.5$ s.

The use of the interface pressure correction p^{int} ($\sigma \geqslant 1$) can effectively stabilize the simulation. As shown in the figure, the void fraction profile is smeared as σ increases, indicating that additional numerical dissipation is introduced, especially in front of the wave. In the rest of our test problems, we will simply set $\sigma = 2.0$.

3.3. Air-to-water shock tube problem

We consider the air–water shock tube problem with nearly pure air and water separated by a diaphragm. A large pressure ratio of 10^4 is imposed across the diaphragm. First, we set the initial condition as follows:

$$(p, \alpha_g, u_i, T_i)_L = (10^9 \text{ Pa}, 1-\epsilon, 0 \text{ m/s}, 308.15 \text{ K}),$$
$$(p, \alpha_g, u_i, T_i)_R = (10^5 \text{ Pa}, \epsilon, 0 \text{ m/s}, 308.15 \text{ K}).$$

where $\epsilon = 1.0 \times 10^{-7}$. Two different meshes of 500 and 5000 cells are used for the computation. The fine mesh solution is used as a reference. The results are presented in Fig. 9.

In this case, the pressure in the air side is much higher than that in the water side. A very strong shock is transmitting into the water, and a rarefaction wave is travelling back into the air. As the sound speed in water is much faster than in air, the speed of shock is much higher than the rarefaction wave. The shock wave, rarefaction wave and the fluid interface are sharply resolved.

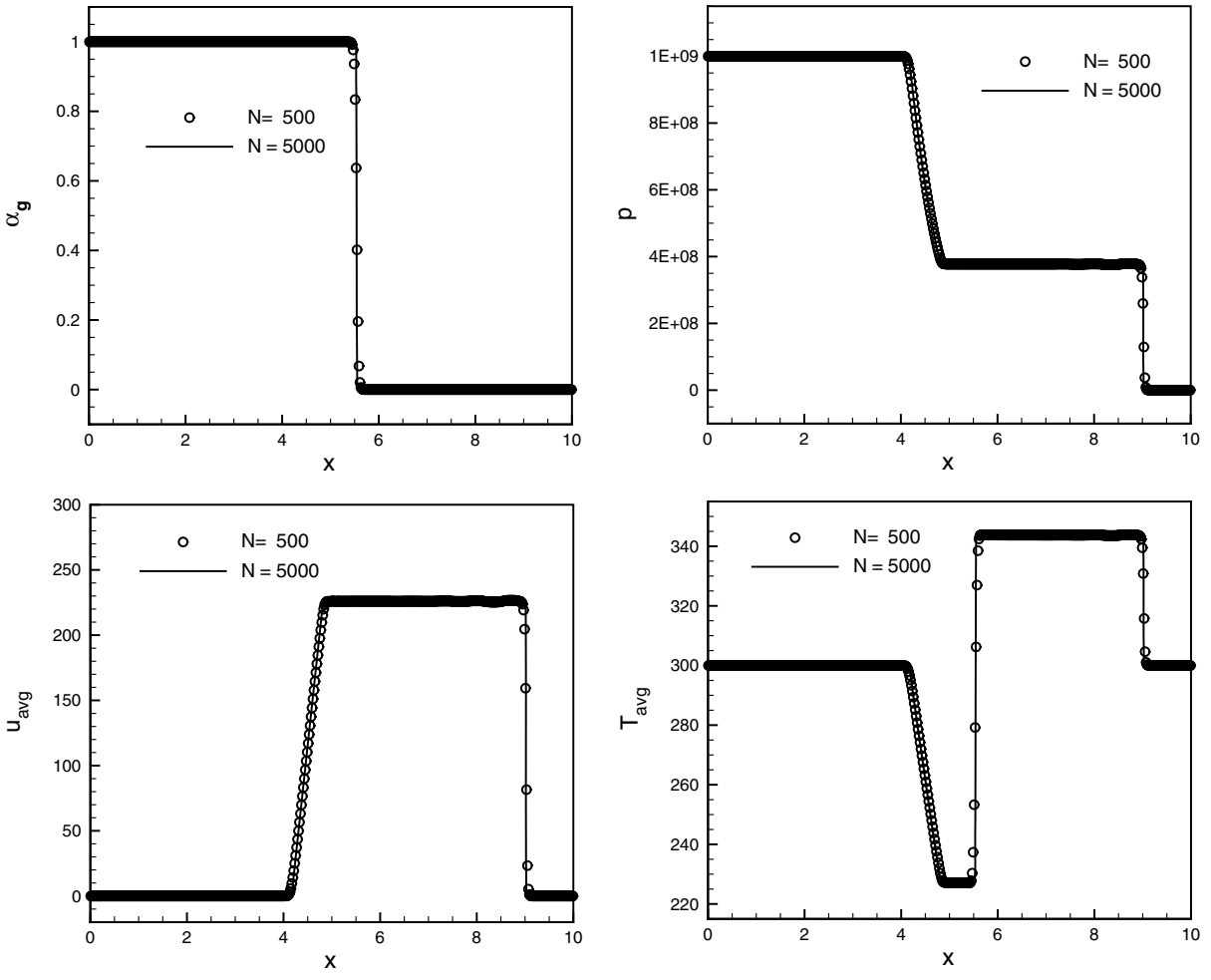

Fig. 9. State profiles for the air–water shock tube problem. The initial condition is $(p, \alpha_g, u_i, T_i)_L = (1.0 \times 10^9, 1-\epsilon, 0, 308.15)$, $(p, \alpha_g, u_i, T_i)_R = (1.0 \times 10^5, \epsilon, 0, 308.15)$, $\epsilon = 1.0 \times 10^{-7}$.

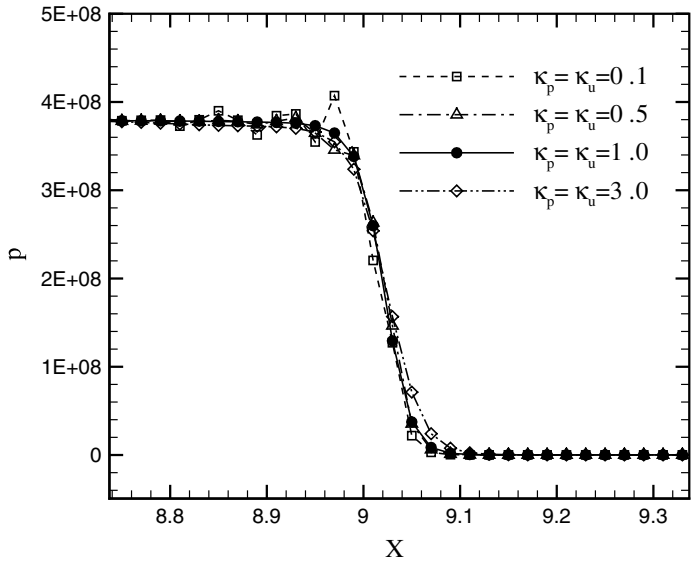

Fig. 10. Effects of diffusion parameters κ_u and κ_p on the solution of the previous air–water shock tube problem.

Next, we use this case to study the influence of diffusion parameters used in the AUSM$^+$-up, namely κ_u and κ_p, on the solution. Fig. 10 shows that a small amount of diffusions, $\kappa_u = \kappa_p = 0.1$, are not sufficient to remove oscillations and a monotonic profile is obtained by setting their values beyond 0.5. The values of $\kappa_u = \kappa_p = 1.0$ appear to be a good balance.

3.4. Water-to-air shock tube problem

Next we change the initial condition so that the shock wave propagates from water to air. We set

$$(p, \alpha_g, u_i, T_i)_L = (1.0 \times 10^7 \text{ Pa}, \epsilon, 0 \text{ m/s}, 308.15 \text{ K}),$$
$$(p, \alpha_g, u_i, T_i)_R = (5.0 \times 10^6 \text{ Pa}, 1 - \epsilon, 0 \text{ m/s}, 308.15 \text{ K}).$$

The results are shown in Fig. 11. It is interesting to note that due to the differences in density and compressibility, it is easy for the shock wave to transmit from air into water as shown in the previous example. On the other hand, it is difficult for the shock to travel from water into air in the sense that a shock wave with only a small pressure ratio is transmitted into air, and a very strong rarefaction is generated from the fluid interface and travelling back into the water. We find that our current method is accurate, providing an improvement in accuracy over our previous method [8] in which a rough scheme was used to represent the flux between unlike phases, as shown in detail by the enlarged insert in the figure. It is also more robust with the current method for a relatively high pressure ratio between water and air. However, it becomes less robust when we increase the pressure ratio to 1000, for example in the case of the following initial condition:

$$(p, \alpha_g, u_i, T_i)_L = (1.0 \times 10^8 \text{ Pa}, \epsilon, 0 \text{ m/s}, 308.15 \text{ K}),$$
$$(p, \alpha_g, u_i, T_i)_R = (1.0 \times 10^5 \text{ Pa}, 1 - \epsilon, 0 \text{ m/s}, 308.15 \text{ K}).$$

As mentioned in Section 2.8, the numerical error in the limit as $\alpha_i \to 0$ is amplified significantly with the large pressure ratio across the rarefaction wave. To avoid divergence in the solution, we need to increase the minimum value of α_i from $\epsilon = 10^{-7}$ to $\epsilon = 10^{-5}$. It is noted that the elevation of the amount of the diminishing phase does not result in a significant impact on the overall behavior of the solution since the magnitude of $\epsilon = 10^{-5}$ is still negligibly small.

We present the results in Fig. 12. The strength of the shock wave in air is much smaller than the rarefaction wave in water; the pressure ratio across the rarefaction wave is about 790 times bigger than the pressure ratio

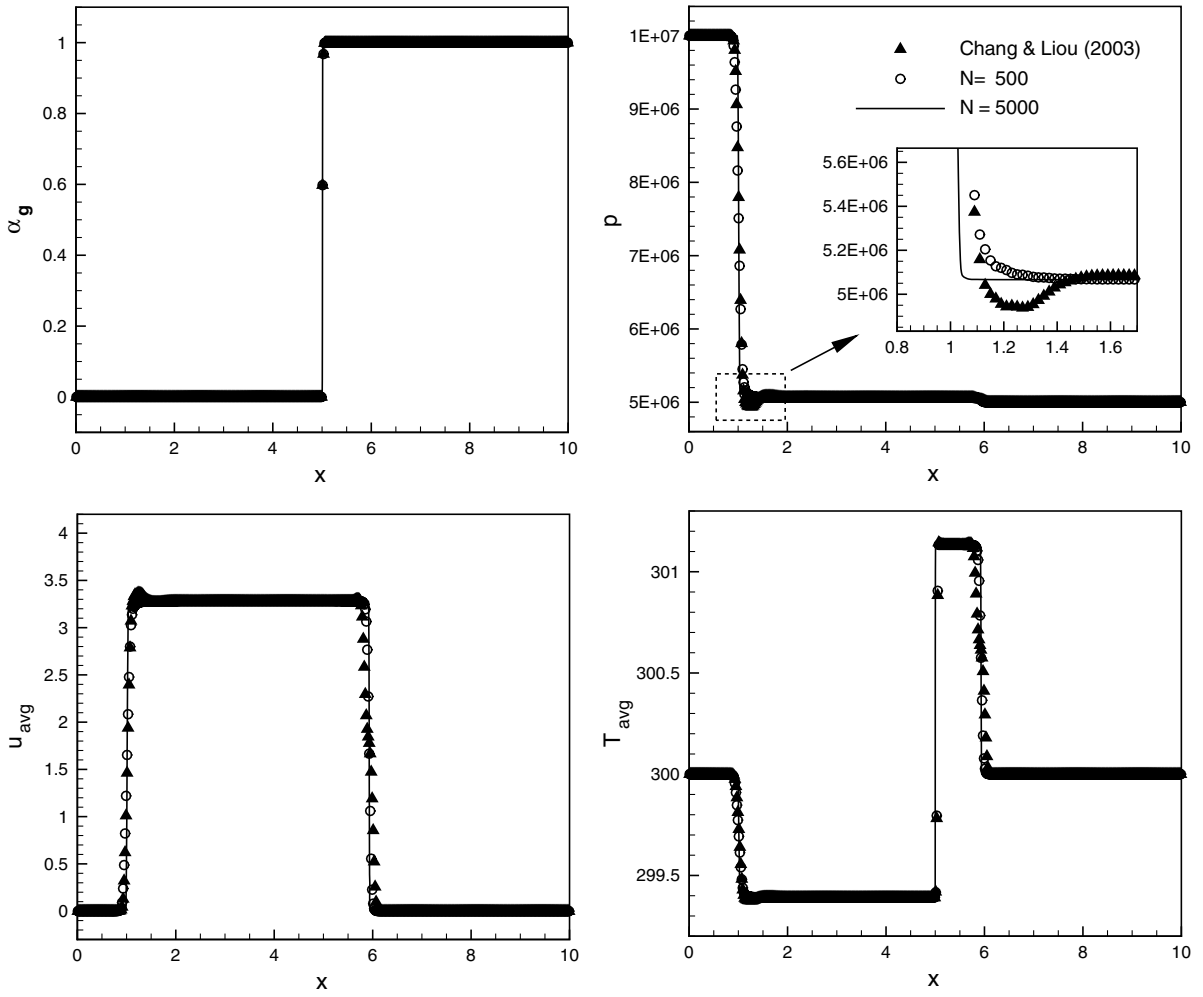

Fig. 11. State profiles for the water–air shock tube problem. The initial condition is $(p, \alpha_g, u_i, T_i)_L = (1.0 \times 10^7, \epsilon, 0, 308.15)$, $(p, \alpha_g, u_i, T_i)_R = (5.0 \times 10^6, 1 - \epsilon, 0, 308.15)$, and $\epsilon = 1.0 \times 10^{-7}$.

across the shock wave in air. Since the shock is too weak to be recognized in the pressure profile, we simply use log scale for the display. It is clear that solutions based on both meshes agree very well.

From the above 1D tests, we may conclude that the AUSM$^+$-up scheme is able to provide accurate and convergent solutions under conditions with large disparities in density, pressure and void fraction, in which the shock and rarefaction waves can be captured well. In what follows, we shall demonstrate its capability for several 2D problems, complicated in flow patterns and rich in flow physics.

3.5. Shock and water–column interaction problem

Here we study phenomena caused by a planar shock wave impinging upon a cylindrical water column. The configuration is shown in Fig. 13. Initially we have a 2D water column with diameter of 3.5 mm located at the origin and an air shock wave set up at $x = -2.0$ mm. The initial condition is given as: before the shock wave,

$$p = 1.0 \times 10^5 \text{ Pa}, \quad u_i = v_i = 0 \text{ m/s}, \quad T_i = 346.98 \text{ K},$$

and the states behind the shock,

$$p = 1.0333 \times 10^6 \text{ Pa}, \quad u_i = 831.48 \text{ m/s}, \quad v_i = 0 \text{ m/s}, \quad T_i = 929.57 \text{ K}.$$

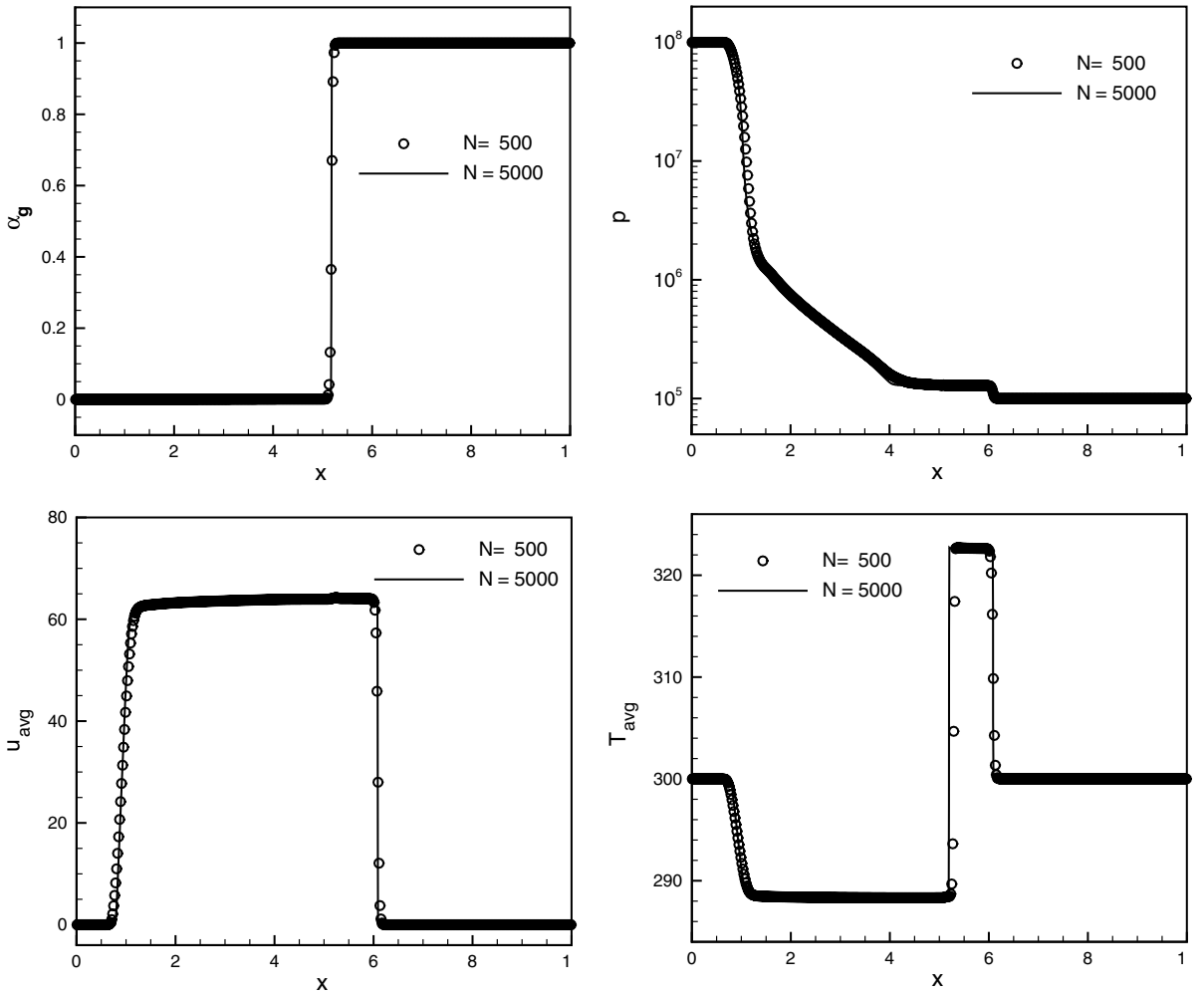

Fig. 12. State profiles for the water–air shock tube problem. The initial condition is $(p, \alpha_g, u_i, T_i)_L = (1.0 \times 10^8, \epsilon, 0, 308.15)$, $(p, \alpha_g, u_i, T_i)_R = (1.0 \times 10^5, 1 - \epsilon, 0, 308.15)$, and $\epsilon = 1.0 \times 10^{-5}$.

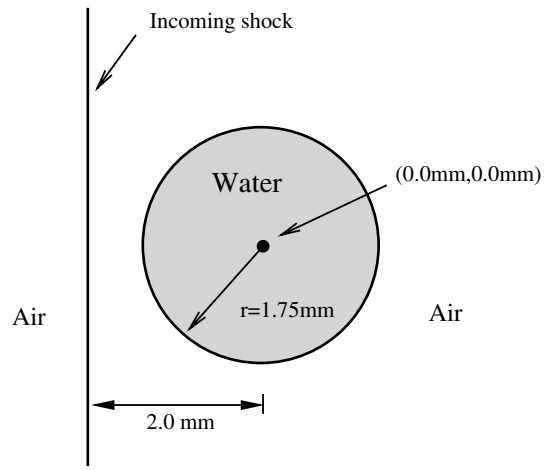

Fig. 13. Illustration of a shock–water column interaction problem.

This yields a shock wave moving at Mach 3 in the air. A mesh of about 670,000 cells is used, covering the domain $[-0.03\text{ m}, 0.04\text{ m}]\times[-0.02\text{ m}, 0.02\text{ m}]$. Fig. 14 shows the time evolution of the simulation result with two different pictures shown side by side for each time frame. One shows the pressure contours together with contour lines of $\alpha_g = 0.1, 0.5$ and 0.9 to identify the fluid interface. The other gives contours of density gradient $\bigtriangledown\rho_{avg}$ (or numerical Schlieren photo). Because of the large difference in compressibility between air and water, we modify the scale of density gradient to accentuate the details of the flow structure. Here, the function $(1+\alpha_1^2)\log(|\bigtriangledown\rho|+1)$ is chosen. We find this modification is able to describe the pressure wave within the water column well.

As in the previous 1D air–water shock tube problem, when the incident shock hits the water column, part of the shock wave is transmitted into the water and part of it is reflected. Since the compressibility of water is much smaller than the air, the shock wave within the water column moves much faster than the shock wave in the air, as evident in (Fig. 14a). When the penetrated shock wave hits the curved interface in the rear of the water cylinder, most of it is reflected as a rarefaction wave, just the opposite of what happens in the front part (or similar to the case of water–air shock tube). The curved interface would act as an "optical" mirror and the reflected rarefaction waves are focused in the rear area, as shown in Fig. 14b and c. The rarefaction waves will be reinforced, eventually creating a low pressure region. As the pressure approaches zero, the air begins to expand and creates a cavitation-like structure in the rear of the water column, even though the air takes only a very small volume fraction in our initial setting ($\alpha_g = 10^{-6}$ within the water[5]). The cavity-like structure can be clearly seen in Fig. 14c–e[6]. While the pressure in the cavitation region continues to drop dramatically (with $p \to 10.0$ Pa in this case), its area is also shrinking smaller and smaller because the surrounding pressure is higher. Eventually the area collapses to a singular point and a shock is generated and propagates outward – a cylindrical shock inside the water column, as seen in Fig. 14f.

In Fig. 14d to f, the incident shock of air glances over the water column and meets in the wake region. It is interesting to note that the foot of the glancing shock continuingly transmits pressure waves into the water column, clearly identifiable with the pressure contours. As the incoming air speed is high and the water speed within the column is close to zero, a strong shear layer (contact discontinuity with a large difference in tangential velocities in this case) is formed in the forward interface. As a result, the interface is getting thicker and thicker, and part of the water appears to be dragged away by the air flow[7].

As we have understood earlier in Section 3.3, the pressure wave in the air transmits into the water easily, but much harder from water to air, due to the mismatch in acoustic impedance. In this case, the pressure wave, once transmitted into the water column, is essentially confined, propagating back and forth, within the water. On the other hand, the pressure field outside of the water column is basically not affected by the waves within water column, with only a very small fraction of the pressure waves being transmitted across the interface. Because the strength of the transmitted waves from the water is very weak, e.g. pressure ratio of 1.013, compared to 10.333 of the incident shock wave, it is too faint to see in the pressure contours. By increasing the image contrast, the shock wave is now visible, as marked by "A" in Fig. 15 in the enlarged view, although the impinging shock is many times more clear. Nevertheless, it demonstrates that our method is capable of resolving well even a faint shock wave, among complicated wave interactions and much stronger waves.

In Fig. 16, we compare the calculated result with the experiment data obtained by Theofanous et al. [29] where a Tributyl Phosphate (TBP) droplet is subject to a Mach 3.0 incident shock wave. Since the material properties (density, viscosity and surface tension coefficient) of TBP is similar to that of water and we are una-

[5] This in fact is not far from reality since water generally contains a slight amount of air.

[6] It is noted that the stiffened gas EOS is not valid at low pressure; in fact, it allows a negative pressure of enormous value, which is clearly not physical. In the real fluid, the water should evaporate when its pressure drops below the vapor pressure. The so-generated vapor would fill the space and prevent the pressure from dropping without limit. Hence, an EOS having the ability to describe phase transition is called for in this situation.

[7] We believe that some of these are the artifacts attributable to numerical dissipations which act more overtly to the contact discontinuity. However, these numerical dissipations covertly compensate for the physical diffusion omitted in our calculation, thus making the qualitative comparison with the reality justifiable.

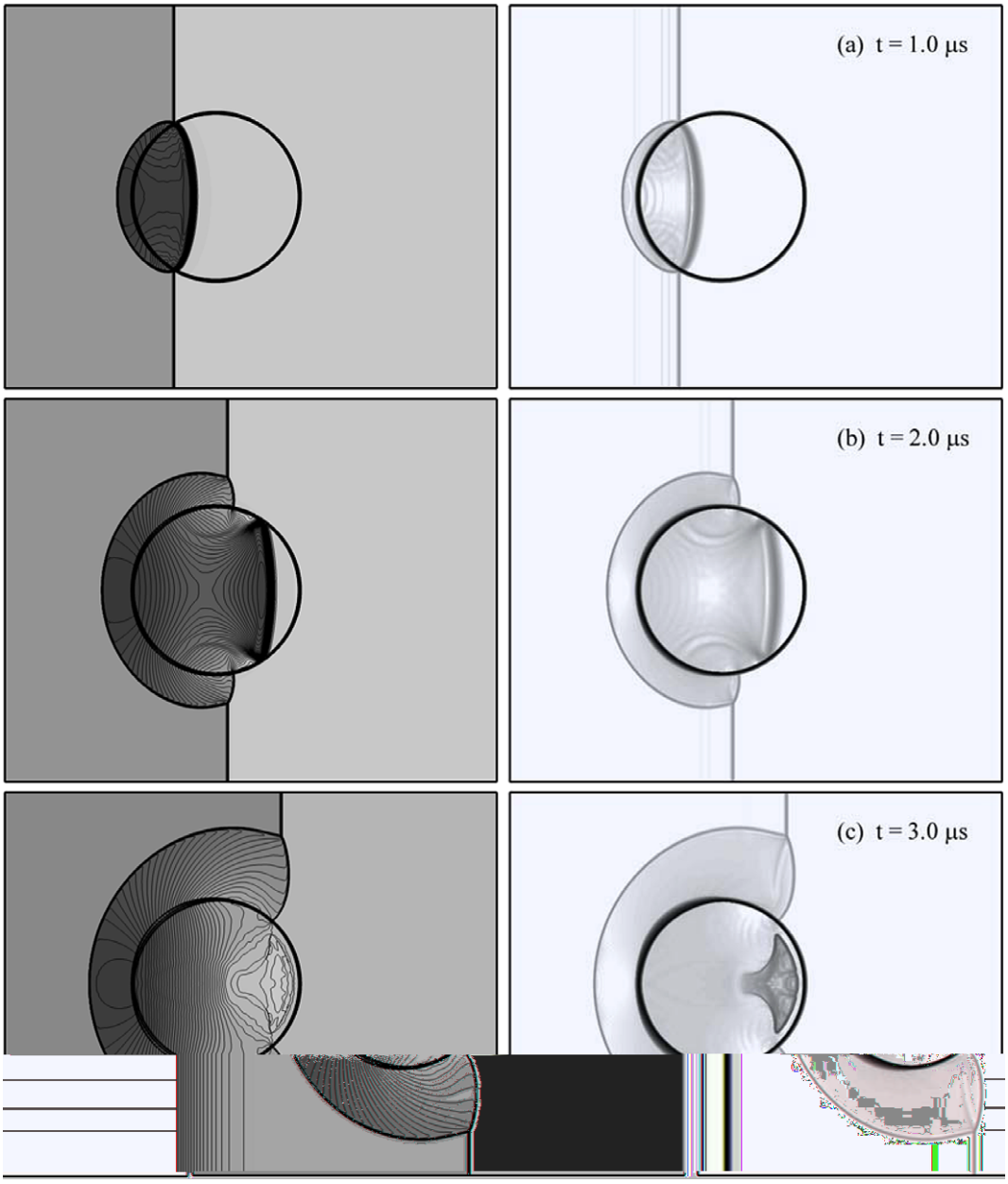

Fig. 14. Time evolution of a shock–water column interaction problem. Incoming shock speed is $M = 3.0$. Left: contours of pressure and void fraction function; Right: contours of function $(1 + \alpha_1^2)\log(|\nabla\rho_{avg}| + 1)$ (Schlieren photo).

ware of other more appropriate EOS, we simply use the water properties for the purpose of a macroscale comparison. Since the Weber number for the TBP droplet is large (We = 30,000), we can safely neglect surface tension. We also ignore the viscous effect which is deemed important in the thin region next to the interface. Nevertheless, the comparison given in Fig. 16 yields an astonishing similarity between the computed and experimental results. It is observed that the shape of droplet is not only changed by the compression force imposed by the incoming air flows, but also equally importantly by the low pressure region created by the reflected rarefaction wave in the rear. As a result, the rear interface is pulled inward. making the droplet rear face flattened. The flattened interface is captured well by the method. This comparison implies that at least at the initial stage the dominant phenomena are basically governed by nonlinear and inviscid mechanisms.

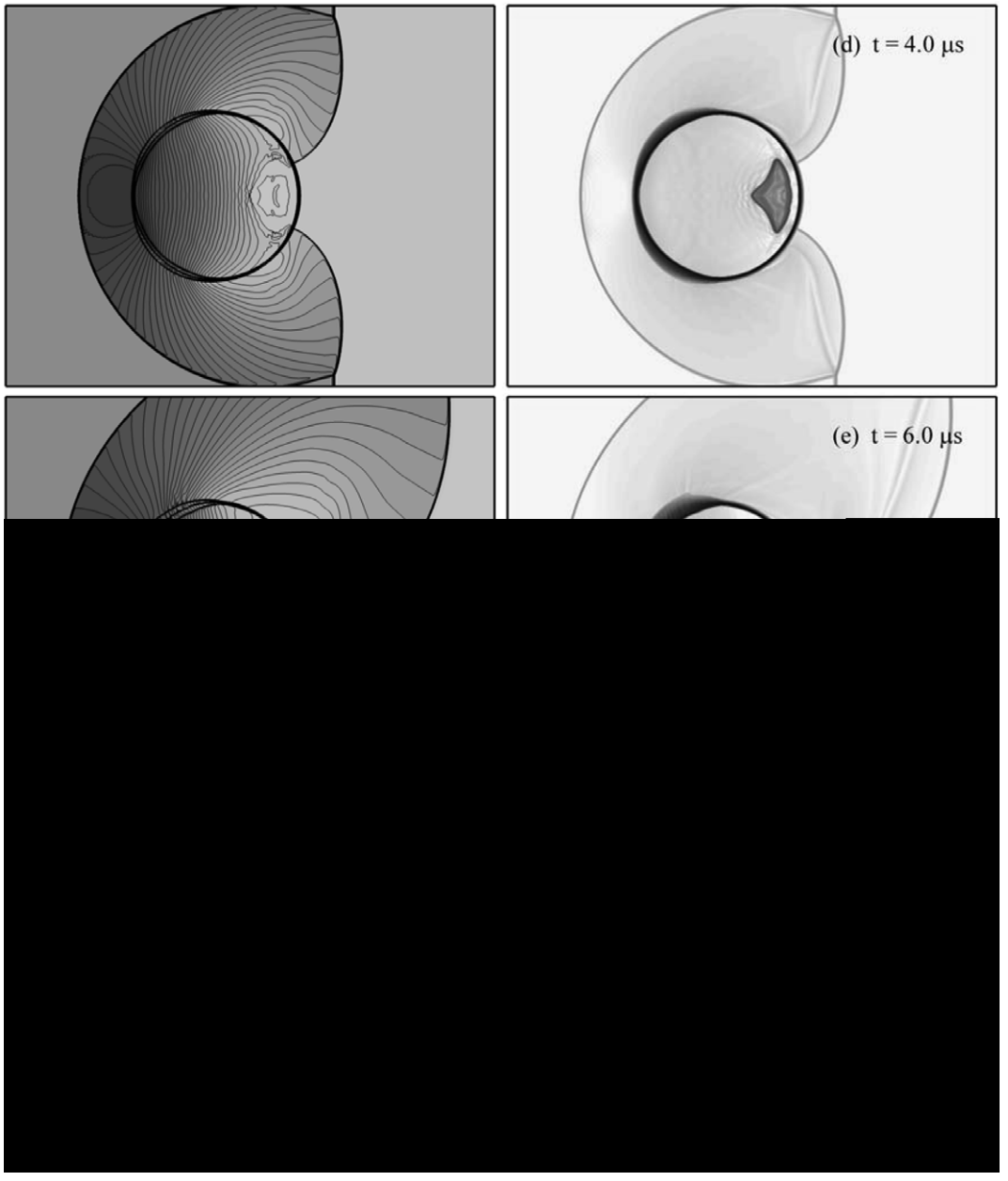

Fig. 14 (*continued*)

Next, we apply our method to a more complicated problem in which two water columns are considered. The geometry of the initial setting is presented in Fig. 17, with an initial condition somewhat different from that of previous case, with the incident shock moving at Mach 6. Hence, we set up the flow parameters for the states before the shock as

$$p = 1.0 \times 10^5 \text{ Pa}, \quad u_i = v_i = 0 \text{ m/s}, \quad T_i = 346.98 \text{ K},$$

while those behind the shock as

$$p = 4.18375 \times 10^6 \text{ Pa}, \quad u_i = 1.818957 \times 10^3 \text{ m/s}, \quad v_i = 0 \text{ m/s}, \quad T_i = 2755.48 \text{ K}.$$

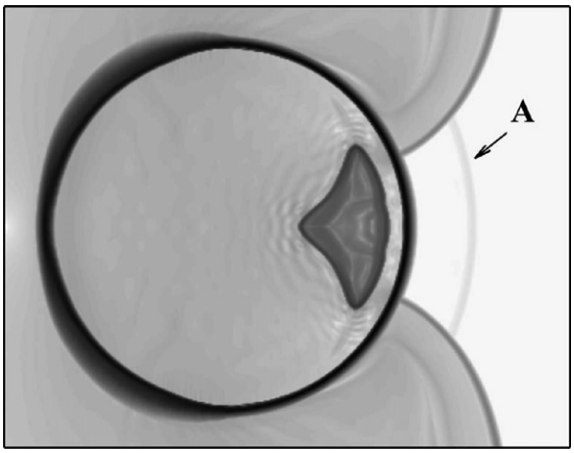

Fig. 15. Enlarged view of numerical Schlieren, corresponding to Fig. 14d at $t = 4.0$ μs, showing the very weak transmitted shock behind the water column and the rarefied region in the rear.

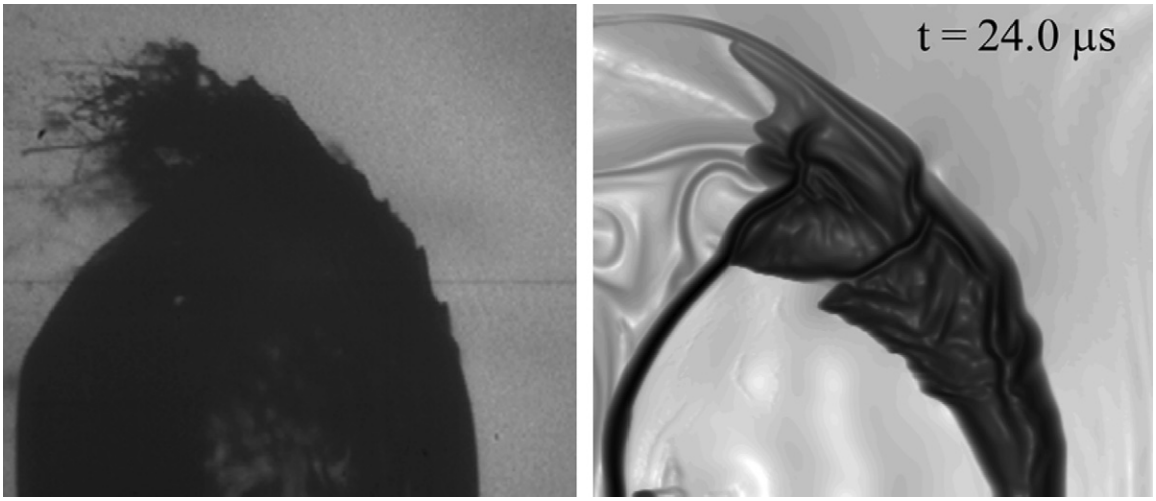

Fig. 16. Schlieren photos for shock-droplet interaction problem. Left: TBP droplet subjected to M = 3.0 flow, We = 30, 000 (Theofanous et al. [29]); Right: numerical result by water droplet with M = 3.0 and We = ∞.

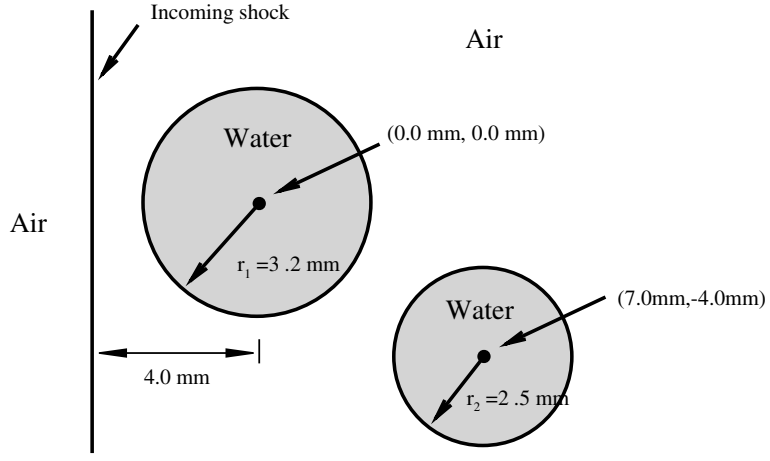

Fig. 17. Illustration of the shock–water column interaction problem. Two water columns case.

The numerical Schlieren photos of the simulation result are shown in Fig. 18. For the first (left) water column, we find in Fig. 18a that the shock wave travels faster outside of the water column than inside, because the sound speed in water is about 4.4 times that in air while the shock Mach number is 6. At the interface facing the incoming flow, the width of the fluid interface increases quickly as shown in Fig. 18b. A complicated flow structure is developed at the interface when the air drags the water away from it, see Fig. 18c–f.

The result shows that after the incoming shock has passed the first water column, the lower part of the shock hits on the second water column (Fig. 18b). The shock is reflected and forms a second bow shock in front of the second column, which in turn transmits into the first water column and modulates the flow field initiated previously by the first incident shock, resulting in asymmetrical profiles, as seen in Fig. 18c–f. The

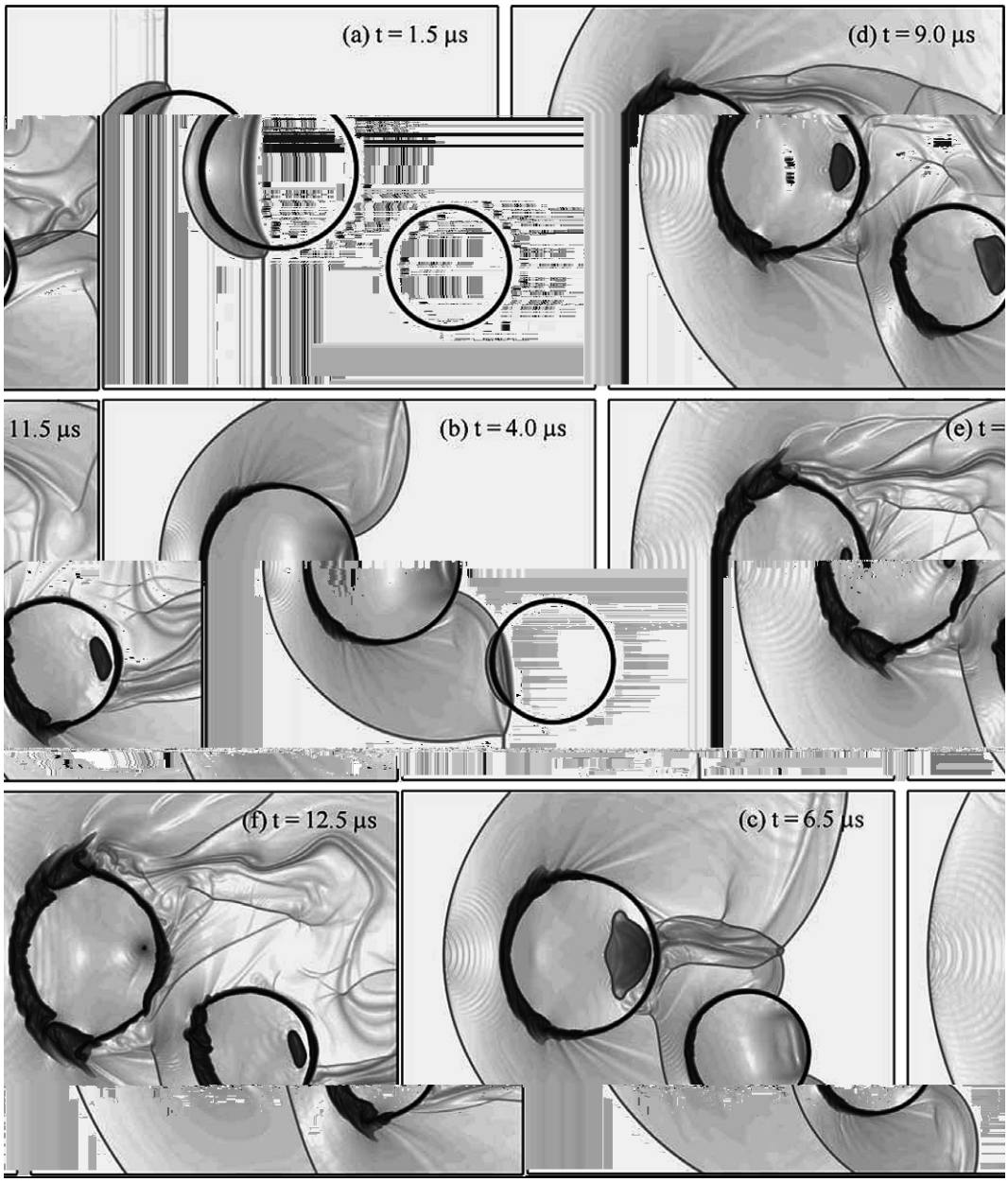

Fig. 18. Time evolution of a shock interacting with two water columns. Contours of function $\log(|\nabla \rho_{\text{avg}}| + 1)$ (numerical Schlieren photo) is presented.

lower and upper parts of the initial shock finally met, see Fig. 18c, in the wake of the first column, creating asymmetric patterns due to the presence of the second column. A very complicated fluid structure is generated in the wake region after the shock passes and the complexities continue to grow. Vortices, shocks, expansion and compression waves, contact lines, etc., all can be clearly seen in the numerical Schlieren photo.

Interestingly, a ripple-like structure is seen, apparently bouncing back and forth between the primary bow shock and the water column.

As in the single column case, a sequence of rarefaction waves make the pressure decrease in the rear region of both columns. Because the incoming shock wave is stronger in this problem than the single column one, the

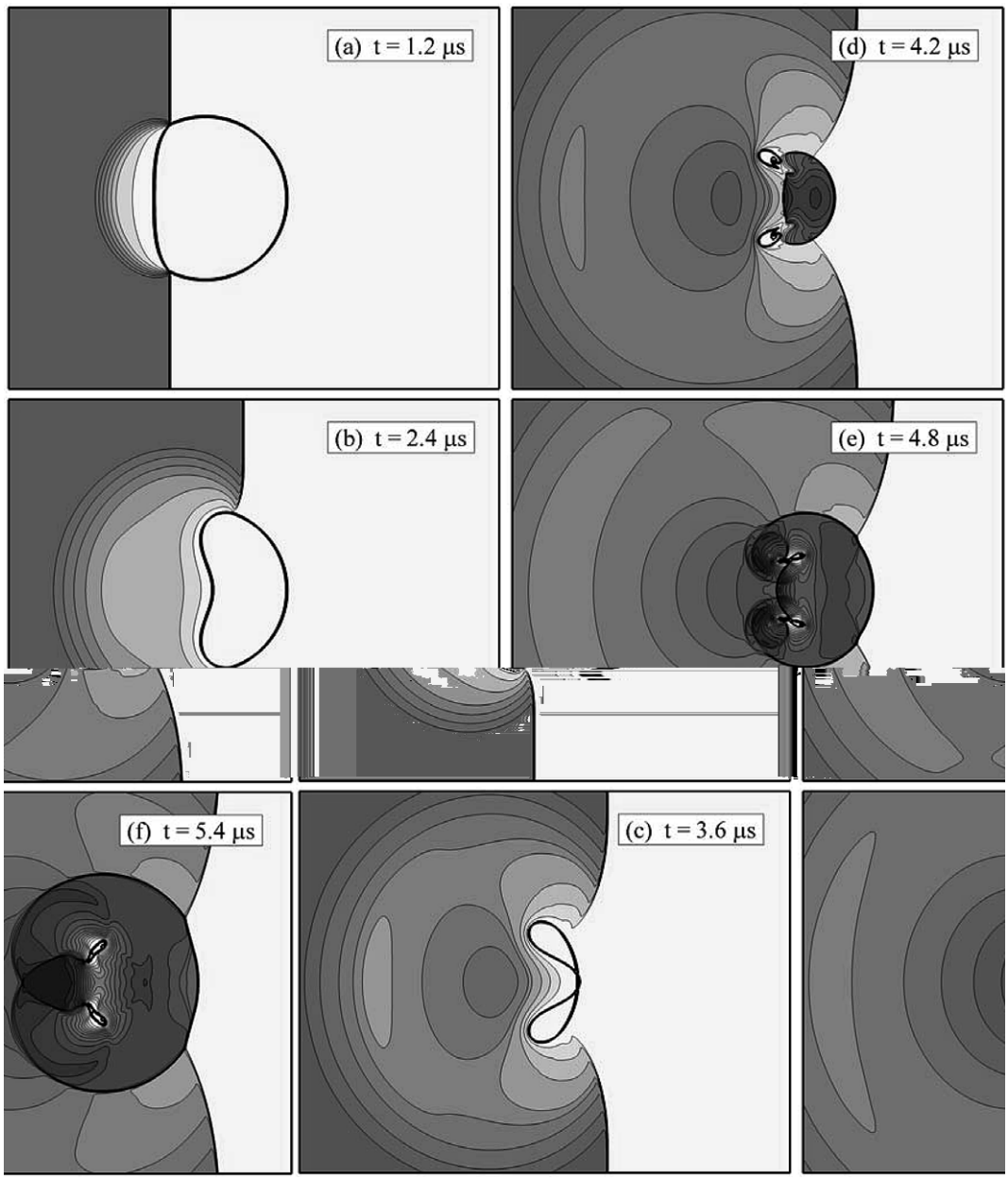

Fig. 19. Pressure and void fraction contours for the shock–bubble interaction problem.

reflected rarefaction wave can drive the pressure to a negative value, hence preventing the calculation of air phase from going forward.

3.6. Shock and air-bubble interaction problem

The interaction of underwater shock wave with air bubble is also studied. The initial condition is the same as that used by Hankin [30]. An air bubble with diameter of 6.0 mm is immersed in the water with its center at the origin. The incoming shock wave initially located at $x = -4.0$ mm is moving at Mach number of 1.509, which is obtained by the following initial conditions. Before the shock wave,

$$p = 1.01325 \times 10^5 \text{ Pa}, \quad u_i = v_i = 0 \text{ m/s}, \quad T_i = 292.98 \text{ K},$$

and behind of the shock wave,

$$p = 1.6 \times 10^9 \text{ Pa}, \quad u_i = 661.81 \text{ m/s}, \quad v_i = 0 \text{ m/s}, \quad T_i = 595.14 \text{ K}.$$

The simulation is performed on a mesh of about 600,000 cells. The time evolution of the simulation result is presented in Fig. 19, showing the contours of pressure and void fraction α_g. We observe that, after the water shock wave hits the bubble, a strong rarefaction wave is reflected back into water from the fluid interface and a relatively weak shock is transmitted into the air ($t = 1.2$–2.4 μs). This is manifested by little variation inside

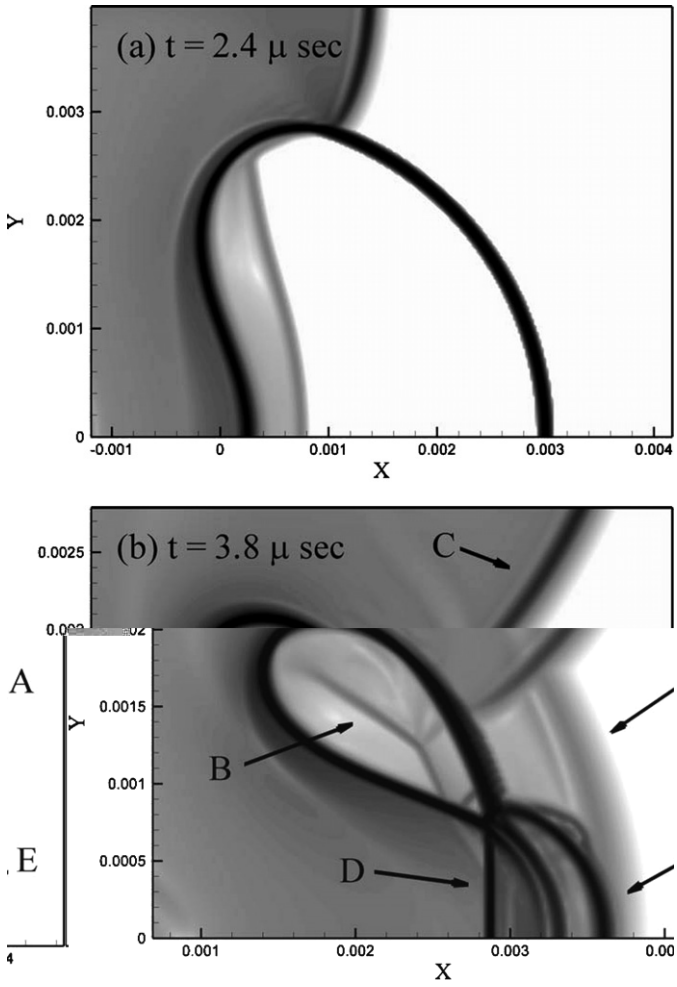

Fig. 20. Numerical Schlieren photo ($\log(|\nabla \rho_{avg}| + 1)$) of shock–bubble interaction problem.

the air bubble, instead the air bubble begins deforming as soon as it is hit by the impinging shock. Again, because of the weak shock wave within the air bubble (no more than 0.1% of strength of the incident shock), it is difficult to identify it in the plot of pressure contours, but more visible in the numerical Schlieren as evident in Fig. 20a.

A water jet generated by the rarefaction wave is formed at the centerline and continuously pushes the bubble into a crescent shape. The speed of the jet can be more than 2000 m/s. As a result, the bubble is finally forced to break up into two separate bubbles and the water jet will collide with the still water behind the bubble at about $t = 3.6\mu$ s (Fig. 19c), thus generating a shock wave which continues to expand radially, as seen in Fig. 19d–f.

As time progresses, the separated air bubbles are compressed into a smaller volume due to the high pressure imposed on it by the surrounding fluids. As the size of the bubble decreases to the local mesh size, the solution becomes under-resolved. Then, additional mesh must be refined or mesh adaptation would be necessary.

Details of the flow are vividly revealed in the enlarged view, shown in Fig. 20b. It consists of several clearly identifiable shock waves: (1) the shock wave transmits across the rear interface from the bubble and enters the water region behind bubble (as indicated by **A**), (2) the shock that is reflected from the rear and still remains within the bubble (indicated by **B**), (3) the incident shock, which has passed over the bubble (indicated by **C**), and (4) the shock waves generated by the high speed water jet (denoted by **D** and **E**). All have been well captured, clearly demonstrating the capability of our method, with no serious smearing found in the result.

3.7. 2D underwater explosion problem

As another example, an underwater explosion problem is computed. This problem is also difficult because it entails a large difference in fluid properties, very strong shock/rarefaction wave, and two fluid interfaces – one being the water free surface and another under the water. Referring to Fig. 21, the initial condition is set as follows: the depth of the water is 1.5 m and a cylindrical core of detonation product is located 1.0 m below the water surface, located at $y = 0$. The diameter of the core is 0.2 m. The fluid states within the core are set as

$$\alpha_g = 1 - \epsilon, \quad p = 1.0 \times 10^9 \text{ Pa}, \quad u_i = v_i = 0 \text{ m/s}, \quad T_i = 2000.0 \text{ K},$$

and the fluid states outside the core are

$$\alpha_g = \begin{cases} \epsilon & \text{if } y < 0, \\ 1 - \epsilon & \text{otherwise}, \end{cases}$$
$$p = 1.0 \times 10^5 \text{ Pa}, \quad u_i = v_i = 0 \text{ m/s}, \quad T_i = 300.0 \text{ K},$$

where $\epsilon = 1.0 \times 10^{-6}$. The computation is performed on a mesh of 760×530 quadrilaterals. Initially, this problem is set up as a 1D cylindrical shock tube problem, in which the high pressure gas of the explosion product in the core is separated from the water by the fluid interface.

We show the time evolution of the simulation result in Fig. 21, in the form of numerical Schlieren photo (contours of $\bigtriangledown\rho_{avg}$). It is noted that $\bigtriangledown\rho_{avg}$ is very large on the fluid interface (about $O(10^7)$ in this case). We need to modify its scale in order to make the flow structure appear more clearly; here, we use the function $(1 + 0.2\alpha_g^5)\log(|\bigtriangledown\rho_{avg}| + 1)$. We also show the contour of $\alpha_g = 0.5$ with a white dash line to mark the location of the fluid interface.

Referring to Fig. 21a, a shock wave is transmitted from the explosion product into the liquid water surrounding the core and propagates radially outward from the core. At the same time, a rarefaction wave is propagating from the core boundary into the center of the core, which can be observed as a pressure drop in the vicinity of the core region by a dark strip inside the core in Fig. 21b. When the shock hits the solid wall at the bottom, it is reflected, generating a high pressure region behind the shock, as seen also in Fig. 21b.

In Fig. 21c, the shock wave hits the upper water surface and pushes it upward. While a small fraction of the shock wave is transmitted into the air, a strong rarefaction wave is reflected from the water surface, propagating downward back to the water and generating a low pressure region near the water surface. Similarly, when the reflected shock from the bottom wall hits the explosion core, a small part of the shock transmits into the

core, which can be clearly seen in the Schlieren, and a rarefaction wave is bounced back from the core interface, producing a low pressure region beneath the core. Since the rarefaction wave is strong, the pressure will drop much more after it has hit the bottom wall and reflected as shown in Fig. 21d.

In Fig. 21e and f, the wave interactions has become progressively more complicated both inside and outside the core. It is noticed that the core has gradually expanded, but essentially retained its shape, because the flow is driven by high pressure in the core, while the shock and air-bubble interactions given in Section 3.6 are unsymmetrically initiated from outside of the air bubble. Again, a faint shock wave transmitted above the water surface is distinguishable and the surface is now deformed noticeably in Fig. 21e and f.

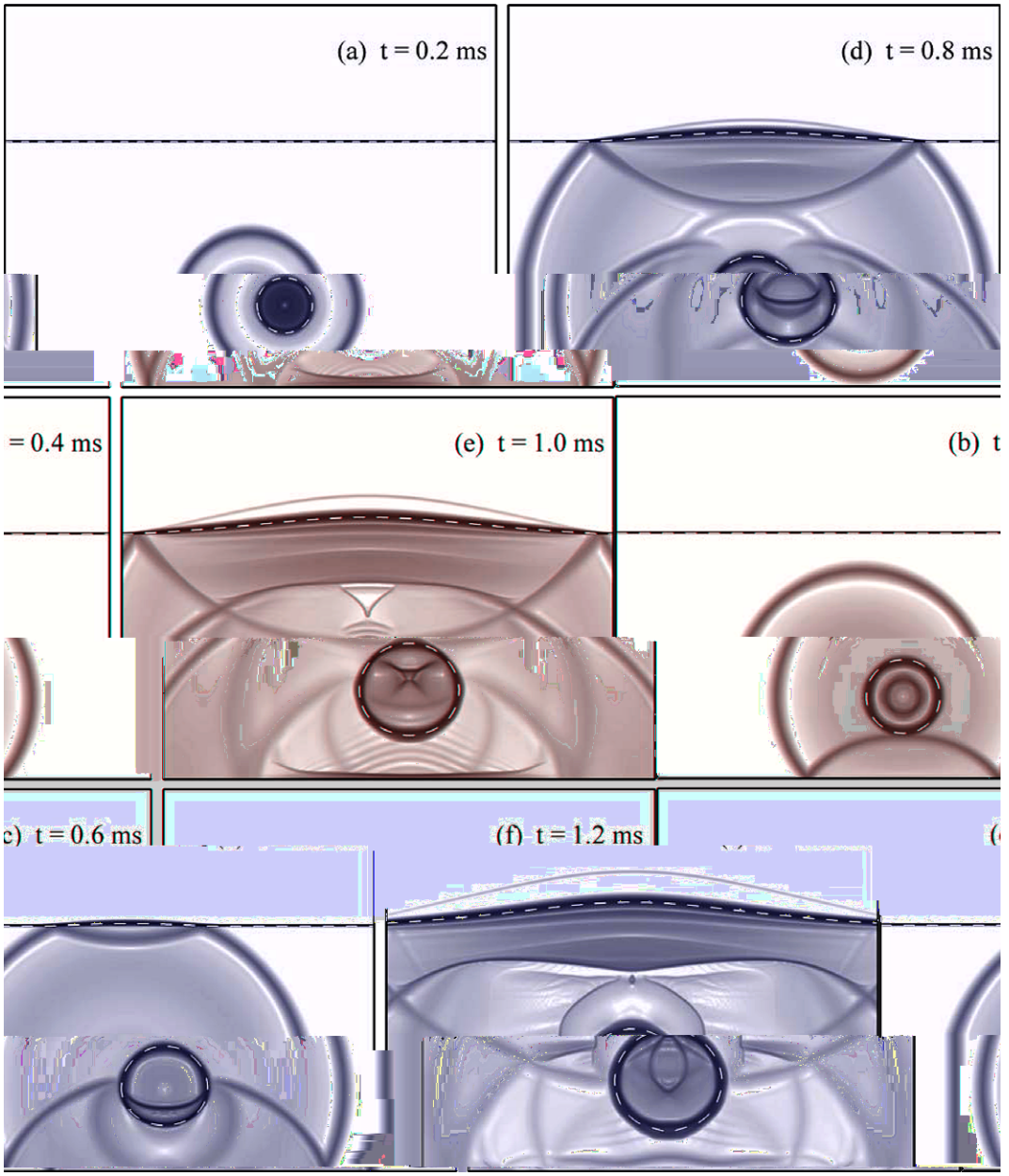

Fig. 21. Time evolution of the underwater explosion problem. Left: Numerical Schlieren photos for underwater explosion problem. The fluid interfaces ($\alpha_g = 0.5$) are outlined by white dashed lines.

4. Conclusion

In this paper, we have proposed a new compressible multiphase multifluid method that makes use of the stratified flow concept. As a result, it is natural to conclude that the numerical fluxes are comprised of two types: interaction of the same fluids, $\mathbf{f}_{g-g}$ and $\mathbf{f}_{l-l}$, and interactions of different fluids, $\mathbf{f}_{g-l}$ and $\mathbf{f}_{l-g}$. This formulation lends itself to satisfy the pressure non-disturbing condition, which is found to be advantageous for capturing discontinuities, such as the fluid interface and shock wave. We extended the recent AUSM$^+$-up method to solve the multifluid equations, where the liquid phase is described by the stiffened gas model. The new method has been applied to a wide variety of one and two dimensional problems. The computed results indicate that our method is accurate and robust, notably for problems with shock-interface interactions, yielding amazingly fine details about complicated interaction phenomena inside the air or water phases, suggesting that the method does not overly smear out even the details of small strength. For a more realistic description of the flow under low pressure, a more accurate description for the liquid phase is needed, together with the capability of handling phase transition.

Acknowledgements

The authors thank the reviewers for their valuable suggestion and comments that have contributed to the improvement of this paper. They are grateful to NASA Glenn Research Center, Cleveland, Ohio, for supporting the research reported herein.

Appendix A. The stiffened gas model

In this paper, the gas and liquid fluids are governed by the perfect gas model and stiffened gas model, respectively. The stiffened gas model proposed by Harlow and Amsden [17] is expressed by

$$p_l = \frac{\gamma_l - 1}{\gamma_l}\rho_l C_{p_l} T_l - p_\infty, \tag{A.1}$$

$$e_l = \frac{C_{p_l}}{\gamma_l} T_l + \frac{p_\infty}{\rho_l}, \tag{A.2}$$

where the parameters $(\gamma_l, C_{p_l}, p_\infty)$ are constants, depending to the material we use. Hence,the speed of sound is simply

$$a_l = \left(\frac{\gamma_l (p_l + p_\infty)}{\rho_l}\right)^{1/2}. \tag{A.3}$$

It is clear that the perfect gas model becomes a special case of the stiffened gas model, by taking $p_\infty = 0$ and a different set of values for γ_l and C_{p_l}. Here, the parameters used for water are determined to meet the following criteria. When $T_l = 293.15$ K and $p = 1.0132 \times 10^5$ Pa, we set the following properties based on the following data:

$$\begin{aligned} &\rho_l = 998.23 \text{kg/m}^3, \\ &C_{v_l} = \left.\frac{\partial e_l}{\partial T_l}\right|_v = 1000 \frac{\text{Cal}}{\text{kg K}} = 4190.0 \frac{\text{J}}{\text{kg K}}, \\ &a_l = 1482 \text{ m/s}. \end{aligned} \tag{A.4}$$

Then, we have

$$\gamma_l = 1.932, \quad C_{p_l} = 8095.08 \frac{\text{J}}{\text{kg K}}, \quad p_\infty = 1.1645 \times 10^9 \text{ Pa}.$$

All the simulations presented in this paper will be based on these parameters. It is remarked that this set of parameters are different from those used by others. In principle, the compressibility factor (ratio of specific heat) γ_l for water should be close to 1.0. The γ_l (=1.932) we use is much closer to 1.0 then 4.4 used by Saurel

and Abgrall [31] and 2.8 used by Paillère et al. [26]. The parameters we choose also give correct density, sound speed and heat capacity in standard atmosphere condition.

The stiffened gas model can provide a reasonable approximation to a fluid in high pressure. Noting that the speed of sound in liquid is substantially higher than that in gas and this fact is accommodated in the equation of state (EOS) by an enormous value of p_∞. As a result of having a large speed of sound, liquid flows usually fall in the low Mach number flow regime and the coupling between the pressure and density fields becomes weak. That is, the variation in density is insignificant even when a very large pressure gradient is imposed on the flow, making the fluid essentially incompressible. On the other hand, small changes in density field can result in huge changes in pressure, making numerical solutions prone to oscillations, due to the presence of a large p_∞ in the EOS. In mathematical terms, the gas–liquid system is said to be stiff.

Appendix B. Exact Riemann solution for the stiffened gas

In what follows we present the exact Riemann solution for the fluid described by the stiffened-gas equation of state. The ideal-gas Riemann solution then becomes a special subset by letting $p_\infty = 0$ and using the corresponding value for γ. The general procedure for constructing the exact Riemann solution is standard. e.g., available in the book by Toro [32]. For completeness, we give the specific formulas for the stiffened gas EOS as described in Appendix A.

We consider a one dimensional Riemann problem, as shown in Fig. 22. The computation domain is divided into four regions by the waves propagating across the domain. The wave associated with the eigenvalues $(u + a)$ and $(u - a)$ can be either a shock wave or a rarefaction wave, and the wave associated with the eigenvalue u is a contact discontinuity. Then we can assign the flow properties in the four regions respectively as $Q_L, Q_L^\star, Q_R^\star$ and Q_R. The Q_L and Q_R are the initial states of the flow on the left and right respectively. The goal is to determine the middle states $Q_L^\star, Q_R^\star$, which are separated by the contact discontinuity, across which we know the following relations.

$$p_L^\star = p_R^\star = p^\star, \tag{B.1}$$

$$u_L^\star = u_R^\star = u^\star. \tag{B.2}$$

These "★" states will be related to the "L" and "R" states through the "$u - a$" and "$u + a$" waves respectively. Across the "$u - a$" wave, we can write the velocity $u^\star$ as a function of Q_L and $p^\star$

$$u^\star = u_L - f_L(p^\star, Q_L), \tag{B.3}$$

with

$$f_L(p^\star, Q_L) = \begin{cases} (p^\star - p_L)\left[\frac{2}{\rho_L((\gamma_L+1)[p^\star+(p_\infty)_L]+(\gamma_L-1)[p_L+(p_\infty)_L])}\right]^{1/2} & \text{if } p^\star \geqslant p_L, \\ \frac{2a_L}{\gamma_L-1}\left[(\xi_L)^{\frac{\gamma_L-1}{2\gamma_L}} - 1\right] & \text{otherwise.} \end{cases} \tag{B.4}$$

And across the "$u + a$" wave, we have a similar relation among $u^\star$, Q_R and $p^\star$, expressed as

$$u^\star = u_R + f_R(p^\star, Q_R), \tag{B.5}$$

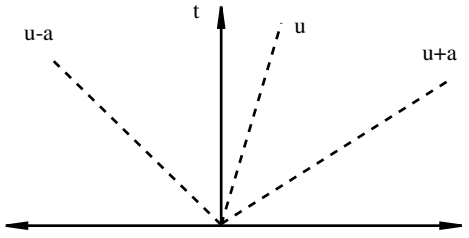

Fig. 22. Illustration of the Riemann problem.

with

$$f_R(p^\star, Q_R) = \begin{cases} (p^\star - p_R)\left[\frac{2}{\rho_R((\gamma_R+1)[p^\star+(p_\infty)_R]+(\gamma_R-1)[p_R+(p_\infty)_R])}\right]^{1/2} & \text{if } p^\star \geqslant p_R, \\ \frac{2a_R}{\gamma_R-1}\left[(\xi_R)^{\frac{\gamma_R-1}{2\gamma_R}}-1\right] & \text{otherwise,} \end{cases} \tag{B.6}$$

and

$$\xi_k = \frac{p^\star + (p_\infty)_k}{p_k + (p_\infty)_k}, \tag{B.7}$$

where the subscript k can be either L or R. From Eqs. (B.3) and (B.5), we get a nonlinear algebraic equation for $p^\star$ as a function of known states Q_L and Q_R,

$$f(p^\star, Q_L, Q_R) = f_L(p^\star, Q_L) + f_R(p^\star, Q_R) + u_R - u_L = 0. \tag{B.8}$$

We use the Newton iteration method to solve for $p^\star$. Then we obtain $u^\star$ by substituting $p^\star$ into Eqs. (B.3) or (B.5). Finally, the densities $\rho_L^\star$ and $\rho_R^\star$ can be calculated from the following equation.

$$\rho_L^\star = \begin{cases} \rho_L\left(\frac{\theta_L\xi_L+1}{\theta_L+\xi_L}\right) & \text{if } p^\star \geqslant p_L, \\ \rho_L(\xi_L)^{\frac{1}{\gamma_L}}, & \text{otherwise,} \end{cases} \tag{B.9}$$

$$\rho_R^\star = \begin{cases} \rho_R\left(\frac{\theta_R\xi_R+1}{\theta_R+\xi_R}\right) & \text{if } p^\star \geqslant p_R, \\ \rho_R(\xi_R)^{\frac{1}{\gamma_R}}, & \text{otherwise,} \end{cases} \tag{B.10}$$

with

$$\theta_k = \frac{\gamma_k + 1}{\gamma_k - 1}. \tag{B.11}$$

Note that the above formulas are for the subsonic case; the ones for supersonic are obtained by simple upwinding, e.g., $p^\star = p_L$ and $u^\star = u_L$ if $u_L - a_L > 0$ and $u_R - a_R > 0$.

References

[1] Y.A. Buyevich, Statistical hydrodynamics for dispersed system, physical background and general equations, J. Fluid Mech. 49 (1971) 489–507.

[2] M. Ishii, Thermo-fluid dynamic theory of two-phase flow, Eyrolles, Paris, 1975.

[3] H.B. Stewart, B. Wendroff, Two-phase flow: models and methods, J. Comput. Phys. 56 (1984) 363–409.

[4] I. Toumi, A. Kumbaro, H. Paillère, Approximate Riemann solvers and flux vector splitting schemes for two-phase flow, Lecture series 1999–03, von Karman Institute for Fluid Dynamics, 1999.

[5] J. Stuhmiller, The influence of interfacial pressure forces on the character of two-phase flow model equations, Int. J. Multiphase Flow 3 (1977) 551–560.

[6] D. Drew, L. Cheng, J.R.T. Lahey, The analysis of virtual mass effects in two-phase flow, Int. J. Multiphase Flow 5 (1979) 233–242.

[7] R. Saurel, R. Abgrall, A multiphase Godunov method for compressible multifluid and multiphase flows, J. Comput. Phys. 150 (1999) 425–467.

[8] C.-H. Chang, M.-S. Liou, A new approach to the simulation of compressible multifluid flows with AUSM$^+$ scheme, AIAA paper 03–4107 (2003).

[9] C.-H. Chang, M.-S. Liou, Simulation of multifluid multiphase flows with AUSM$^+$-up scheme, in: Third Internation Conference of Computational Fluid Dynamics, Toronto, Canada, 2004.

[10] R. Abgrall, R. Saurel, Discrete equations for physical and numerical compressible multiphase mixtures, J. Comput. Phys. 186 (2003) 361–396.

[11] R. Saurel, S. Gavrilyuk, F. Renaud, A multiphase model with internal degrees of freedom: application to shock–bubble interaction, J. Fluid Mech. 495 (2003) 283–321.

[12] O. LeMétayer, J. Massoni, R. Saurel, Modeling evaporation fronts with reactive Riemann solvers, J. Comput. Phys. 205 (2005) 567–610.

[13] B. Van Leer, Flux vector splitting for the Euler equations, in: Proceedings of the 8th International Conference on Numerical Methods in Fluid Dynamics, Springer Verlag, Berlin, 1982.

[14] M.-S. Liou, Ten years in the making – AUSM-family, AIAA paper 2001–2521, in: 15th Computational Fluid Dynamics Conference Proceedings, 2001.
[15] M.-S. Liou, A sequel to AUSM: AUSM$^+$, J. Comput. Phys. 129 (1996) 364–382.
[16] M.-S. Liou, J.R. Edwards, Numerical speed of sound and its application to schemes for all speeds, AIAA paper 99–3268 (1999).
[17] F. Harlow, A. Amsden, Fluid dynamics, Technical Report LA-4700, Las Alamos National Laboratory, 1971.
[18] M.-S. Liou, A further development of the AUSM$^+$ scheme toward robust accurate solution for all speed, AIAA paper 2003–4116, in: 16th Computational Fluid Dynamics Conference Proceedings, 2003.
[19] M.-S. Liou, A sequel to AUSM, part II: AUSM$^+$-up for all speeds, J. Comput. Phys. 214 (2006) 137–170.
[20] J.R. Edwards, M.-S. Liou, Low-diffusion flux-splitting methods for flows at all speeds, AIAA Journal 36 (9) (1998) 1610–1617.
[21] G. Wallis, One-dimensional two-phase flow, McGraw-Hill, New York, 1964.
[22] W. Hancox, R. Ferch, W. Liu, R. Nieman, One-dimensional models for transient gas–liquid flows inducts, Int. J. Multiphase Flow 6 (1980) 25–40.
[23] I. Toumi, An upwind numerical method for two-fluid two-phase flow models, Nuclear Sci. Eng. 123 (1996) 147–168.
[24] S.K. Godunov, Numerical solution of multidimensional gas dynamics problems, Nauka, Moscow, 1976.
[25] M.-S. Liou, L. Nguyen, C.-H. Chang, S. Sushchikh, R. Nourgaliev, T. Theofanous, Hyperbolicity, discontinuities, and numerics of two-fluid models, Technical report, Springer, in: 4th International Conference on Computational Fluid Dynamics, 2006.
[26] H. Paillère, C. Corre, J.R.G. Cascales, On the extension of the AUSM$^+$ scheme to compressible two-fluid models, Comput. Fluids 32 (2003) 891–916.
[27] S.R. Chakravarthy, S. Osher, Computing with high-resolution upwind schemes for hyperbolic equation, Lect. Appl. Math. 22 (1985) 57–86.
[28] V.H. Ransom, Numerical benchmark tests, in: G.F. Hewitt, J.M. Delhaye, N. Zuber (Eds.), Multiphase Science and Technology, vol. 3, Hemishpere Publishing Corporation, 1987.
[29] T. Theofanous, G. Li, T. Dinh, Aerobreakup in rarefied supersonic gas flows, J. Fluids Eng. 126 (2004) 516–527.
[30] R.K.S. Hankin, The Euler equations for multiphase compressible flow in conservation form: simulation of shock–bubble interactions, J. Comput. Phys. 172 (2) (2001) 808–826.
[31] R. Saurel, R. Abgrall, A simple method for compressible multifluid flows, SIAM J. Sci. Comput. 21 (3) (1999) 1115–1145.
[32] E.F. Toro, Riemann solvers and numerical methods for fluid dynamics: a practical introduction, Springer-Verlag Telos, 1997.